CR 73234

AVAILABLE TO THE PUBLIC

GPO PRICE $ _____

CSFTI PRICE(S) $ _____

Hard copy (HC) 3.00

Microfiche (MF) .65

ff 653 July 65

CR 73234
AVAILABLE TO THE PUBLIC

DESIGN STUDY OF A FOURIER SPECTROMETER-ELLIPSOIDAL MIRROR REFLECTOMETER SYSTEM

FINAL REPORT

PREPARED BY: G.J. KNEISSL of

DUNN ASSOCIATES, INC.
11601 NEWPORT MILL RD.
SILVER SPRING, MD. 20902

PREPARED FOR: NASA AMES RESEARCH CENTER
MOFFET FIELD
CALIFORNIA 94035

UNDER CONTRACT NAS 2-4232

DATE: June 10, 1968

TABLE OF CONTENTS

1.0 Introduction

The purpose of this investigation was to optimize a reflectometer system consisting of a fast scanning Michelson Interferometer and an ellipsoidal mirror reflectometer. The system should be capable of measuring the reflectance of opaque materials at room temperature with an accuracy of 1% full scale and should cover the wavelength range from 2 to 40μm. To accomodate this wavelength range two optical heads (two Michelson interferometers) would be used. One would work in the wavelength range from 2 to 12μm while the second one would cover the range from 10 to 40μm.

Figure 1 shows a schematic of the Fourier spectrometer-ellipsoidal mirror reflectometer system.

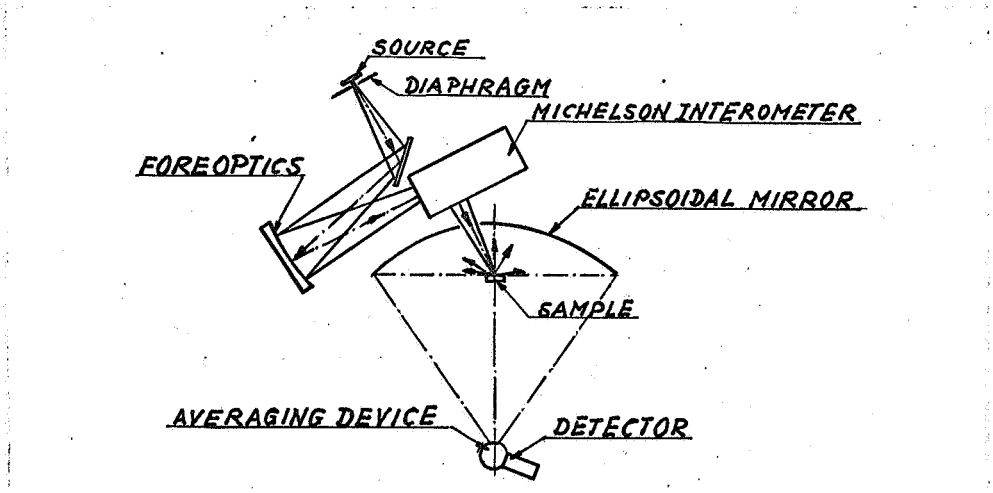

Fig. 1 Interferometer - EMR system

The foreoptics focus the beam through the Michelson interferometer and image a portion of the source, as defined by a diaphragm, onto the sample. The reflected flux is collected by the ellipsoidal mirror and focused onto the detector at the second focal point of the mirror.

In the following sections 1.1 and 1.2 we will examine some components of the system.

1.1 The Michelson interferometer.

In this section a few characteristics of the scanning interferometer will be discussed but only to the extent necessary to understand the later sections of this report. The reader interested in the theory of Fourier transform spectroscopy should consult the publications by J. Connes[1], L. Mertz[2] or references contained therein. The following considerations are mainly taken from a technical report by L.W. Chaney.[3]

An outline sketch of the basic interferometer is given in Figure 2. The basic operation is as follows: The input radiation represented by the ray B is divided at the beam splitter into two rays B_1 and B_2; each ray is returned to the beam splitter and divided again. Two recombined beams are thus formed. One recombined beam is reflected back towards the input and lost while the other beam passes through the lens and is focused on the aperture plate and detector. The moving mirror is displaced through a distance $\pm$ L/2 from a point of zero retardation such that the optical path difference is equal to $\pm$ L.

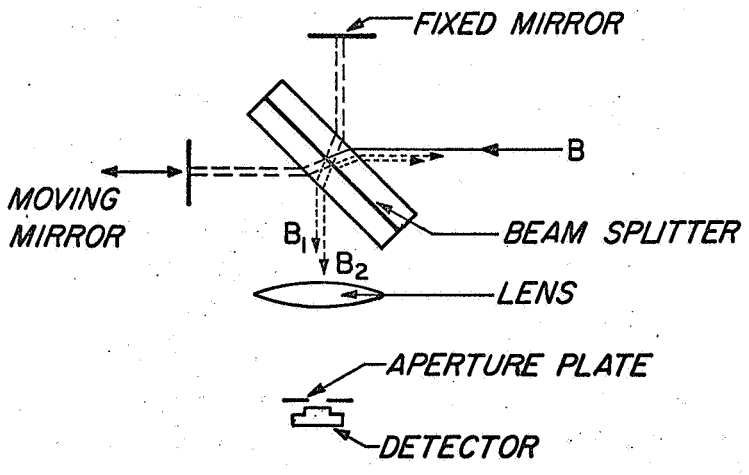

Fig. 2 Basic Interferometer

Assuming that the mirror moves at a constant velocity V the interferometer modulates each wavelength sinusoidally. The modulation frequency f is characteristic for each wavelength and is given by

$$f = \frac{2V}{\lambda} \qquad (1)$$

where V is the velocity of the scanning mirror in μm/sec as mentioned above and λ is the wavelength in μm.

The use of the interferometer has two basic advantages over the conventional grating or prism spectrometers.

a) Fellgett's advantage.

The basis of this advantage is that in observing a spectral element the increase in signal to noise ratio, S/N, is proportional to the square root of the elemental observation time T. If the different spectral elements are explored consecutively, as is done in a conventional spectrometer, the time available for each spectral element is t = T/M, where M is the number of spectral elements. The interferometer, however, observes all the spectral elements for the total time T. The signal to noise ratio is therefore increased by the factor $\sqrt{M}$.

b) The Throughput Advantage.

The throughput (TP) of an optical instrument is a measure of the amount of light transmitted by an instrument having a given aperture and a given solid angle. For an instrument with no optical losses TP is given as

$$TP = A\Omega$$

where A is the area of the aperture and Ω the solid angle.

For any spectrometer the permissible solid angle is limited since an increase in solid angle will decrease the spectral resolution. Thus, the product of the resolution R and the solid angle Ω

is a constant. The product $R\Omega$ for an interferometer is much larger (two orders of magnitude) than in a grating spectrometer.

Interferometer $R\Omega = 2\pi$

Grating Spectrometer $R\Omega = 0.07$

Unfortunately, as will be evident later, a Fourier transform-ellipsoidal mirror reflectometer system can only make very limited use of the TP advantage.

1.2 The ellipsoidal mirror reflectometer (EMR).

The EMR has been described in detail by Dunn[4] et al. Only the features important to this study will be given here. A schematic of the EMR is shown in Fig. 3.

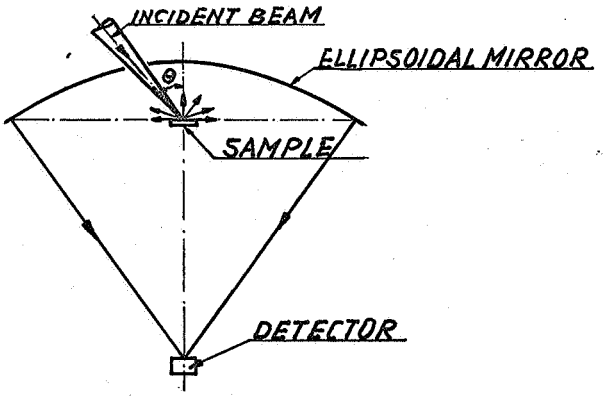

Fig. 3 Basic Ellipsoidal Mirror Reflectometer

The sample is located at the first focal point. A beam enters the ellipsoidal mirror through a hole and is incident on the sample under a polar angle θ. The irradiated area and the solid angle under which the sample sees the entrance hole determine the throughput. As discussed by S.T. Dunn[4] the entrance hole has to

be kept small if high accuracy is desired and the irradiated area on the sample is limited too. The throughput of the reflectometer therefore does not allow one to make use of the high throughput of the interferometer. The reflected flux is focused by the ellipsoidal mirror on a suitable detector placed at its second focal point. Since the flux contained in a beam has to stay constant in a lossless optical system the smaller solid angle under which the beam strikes the detector is accompanied by an image magnification. For the ellipsoidal mirror used in the NBS reflectometer the linear magnification was about 6x.

The flux distribution over the image at the second focal point will vary greatly with the directional distribution of the reflected flux from the sample. Therefore large errors can occur if the responsivity changes across the sensitive area of the detector. Another source of error as far as the detector is concerned is an angular variation of responsivity within the field of view of the detector. For the NBS reflectometer the total field of view was approximately 60°. While the uniform angular responsivity is reasonably well fulfilled for the FOV specified above the nonuniform spatial responsivity does present a problem. Therefore it is necessary to use an averaging device in front of the detector if highly accurate data are desired.

The averaging device to be used with the EMR should make efficient use of the available flux in order not to lower the signal to noise ratio to the extent where measurements are no longer possible. S.T. Dunn[5] investigated several methods of flux averaging in the infrared. He found that from the standpoint of averaging, a small sulfur coated integrating sphere was the best solution to the problem. A new approach to eliminate spatial variations of responsivity was described by M. Finkel.[6] He proposed detector scanning as a way to eliminate this problem. It should be

mentioned at this point, that detector scanning does not correct for the directional nonuniformity of the detector which means that directional insensitive detectors have to be used if detector scanning is employed.

For reflectance measurements in the infrared it becomes important to discriminate between emitted and reflected flux even if the sample is only at room temperature because the emitted flux becomes an appreciable fraction of the reflected flux. In a conventional system this is done by chopping the incident flux by a mechanical chopper and by amplifying the signal with a tuned ac-amplifier. Since the Michelson interferometer modulates each wavelength with its own-characteristic frequency it acts as a chopper. In this case it is necessary to employ a broadband ac-amplifier since it has to amplify all frequencies which correspond to the wavelength range passed by the interferometer. The possibility to use the interferometer as an optical chopper has been described by S.T. Dunn.[7]

2.0 Comparison between averaging by the use of an averaging sphere and detector scanning.

In section 1 it had been established that an efficient as well as accurate method of averaging is the crucial point for obtaining accurate reflectance data with an EMR. In the following sections 2.1 and 2.2 we will discuss and compare the two most promising methods of averaging, the use of an averaging sphere and the employment of detector scanning.

2.1 The averaging sphere.

2.1.1 Theory of the averaging sphere.

The following equations will be derived using the assumption that

a) the coating is a perfectly diffuse reflector of uniform reflectance

b) the entrance and detector ports are perfect absorbers (ρ=0)

c) perturbations caused by the shield will be neglected.

The following symbols will be used:

ϕ_o flux, entering the averaging sphere initially

ρ_w reflectance of the sphere coating

A_E area of the entrance port

A_I area of the image (it is assumed that the beam is focused on the entrance port.) $A_I < A_E$

A_D area of the detector (also area of the detector port.)

A_V area of the sphere viewed by the detector

A total sphere area

As shown in Fig. 4 the flux ϕ_o is entering the sphere and strikes the sphere wall at a location which is shielded from the detector's field of view. The flux leaving the sphere wall is $\rho_w \phi_o$. The flux incident on A_V is $(A_V/A)\rho_w \phi_o$ and the first portion of flux incident on the detector, $\phi_{D,1}$, is

$$\phi_{D,1} = \frac{A_D}{A} \frac{A_V}{A} \rho_w^2 \phi_o .$$

The flux lost after the first reflection is $\rho_w \phi_o (A_E + A_D)/A$ which leaves $\rho_w \phi_o \left[1 - (A_E + A_D)/A\right]$ in the sphere. This flux is again reflected off the spherewall and the fraction A_V/A is incident on the detector's field of view.

The flux falling on the detector after three reflections on the sphere wall have occurred becomes

$$\phi_{D,2} = \frac{A_D}{A} \frac{A_V}{A} \rho_w^3 \frac{A - (A_E + A_D)}{A} .$$

By calculating the amount of flux incident on the detector after each reflection on the sphere wall we end up with an infinite

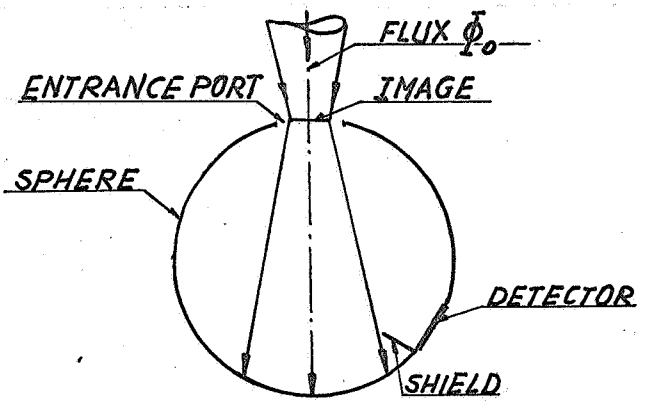

Fig. 4 Configuration of Averaging Sphere

series as follows:

$$\phi_D = \frac{A_D A_V}{A^2} \rho_W^2 \phi_0 \left[1 + \rho_W \left(1 - \frac{A_E + A_D}{A} \right) + \rho_W^2 \left(1 - \frac{A_E + A_D}{A} \right)^2 + \ldots \right] .$$

This is a converging geometric series which converges to

$$\phi_D = \frac{1}{A} \frac{A_D A_V \rho_W^2 \phi_0}{A - \rho_W \left[A - (A_E + A_D) \right]} .$$

2.1.2 Efficiency of an averaging sphere.

We obtain a measure of efficiency by comparing the signal to noise ratio we would get for two cases. For the first case we will place the detector directly into the beam, while for the second case an averaging sphere will be used.

Assuming a uniform flux density at the second focal point the flux incident on the detector without averaging sphere would be $\phi_0 \frac{A_D}{A_I}$. To find the signal to noise ratio we have to divide the available power by the noise equivalent power or

$$\left(\frac{S}{N} \right)_1 = \phi_0 \frac{A_D}{A_I} \frac{1}{NEP_\lambda} = \phi_0 \frac{A_D}{A_I} D_\lambda$$

where D_λ is called the spectral detectivity. The detector parameter normally given is D^*_λ which is a normalization of the spectral detectivity to take into account the area and the electrical bandwidth dependence or

$$D^*_\lambda = \sqrt{A_D \Delta f}\, D_\lambda .$$

Using this expression the signal to noise ratio, when the beam is directly incident on the detector, $\left(\frac{S}{N}\right)_1$, becomes

$$\left(\frac{S}{N} \right)_1 = \phi_0 \frac{A_D}{A_I} \frac{D^*_\lambda}{\sqrt{A_D \Delta f}} = \frac{\phi_0}{A_I} \frac{\sqrt{A_D}\, D^*_\lambda}{\sqrt{\Delta f}} .$$

Using the same derivation we obtain the signal to noise ratio when the averaging sphere is used, $(S/N)_2$, as

$$\left(\frac{S}{N}\right)_2 = \frac{1}{A}\,\frac{A_D A_V \rho_w^2 \phi_0}{A - \rho_w\left[A - (A_E + A_D)\right]}\,\frac{D_\lambda^*}{\sqrt{A_D \Delta f}} .$$

Since we are concerned with an order of magnitude calculation we can make the simplifying assumption that the detector is essentially seeing the entire sphere or that $A_V \approx A$. With this we obtain

$$\left(\frac{S}{N}\right)_2 = \frac{\sqrt{A_D}\,\rho_w^2 \phi_0}{A - \rho_w\left[A - (A_E + A_D)\right]}\,\frac{D_\lambda^*}{\sqrt{\Delta f}}$$

The efficiency of the averaging sphere, $(S/N)_2 / (S/N)_1$, becomes

$$\frac{(S/N)_2}{(S/N)_1} = A_i\,\frac{\rho_w^2}{A - \rho_w\left[A - (A_E + A_D)\right]} .$$

This result will be used later to compare the averaging sphere with detector scanning.

2.2 Image (detector) Scanning.

2.2.1 Theory of detector scanning.

The approach used in this paragraph which is different from that used by Finkel[6] is partially taken from a paper by Geist and Kneissl.[8] As indicated in Fig. 5 assume that the flux density at a cross section of a beam can be described by a function defined as

$A = A(x', y')$ for all (x', y') which belong to the closed rectangle $R' \{0 \le x' \le a;\ 0 \le y' \le b\}$

and $A = 0$ for all (x', y') not contained in R' .

Likewise assume that the local responsivity of a detector can be described by a function such that

$B = B(x,y)$ for all (x,y) which belong to the closed rectangle $R\{0 \le x \le c, 0 \le y \le d\}$

and B = 0 for all (x,y) not contained in R.

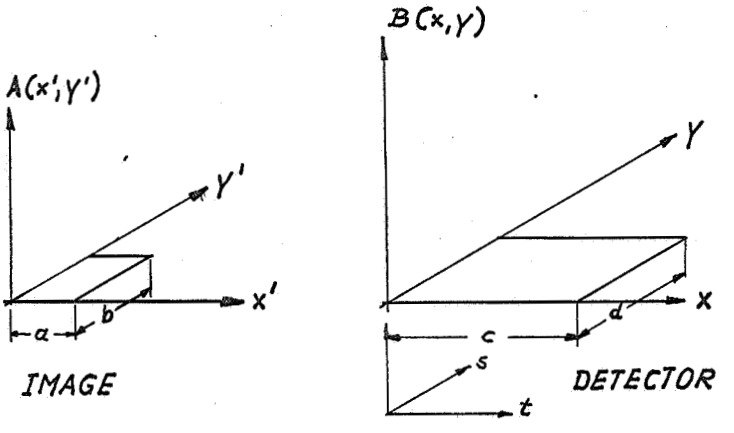

Fig. 5 Basic parameters for detector scanning

In addition we need a coordinate system (s,t) which describes the location of the image on the detector.

As shown in Fig. 6 the detector is scanned in a raster pattern

at a constant velocity. The raster spacing is Δs . It should be noted that the raster sweep must start and end with the image completely in the detector area. We denote the time integral of the detector output signal over the period of the scan by I. It will be the task of the following derivation to show that in the limit as Δs approaches zero, I becomes the product of two integrals. The first integral gives the total flux contained in the beam while the second is the integral over the local responsivity of the detector which is a constant for any given detector. Thus the ratio of two scans, I_1 / I_2 , becomes the ratio of the fluxes contained in the two beams which is the desired quantity.

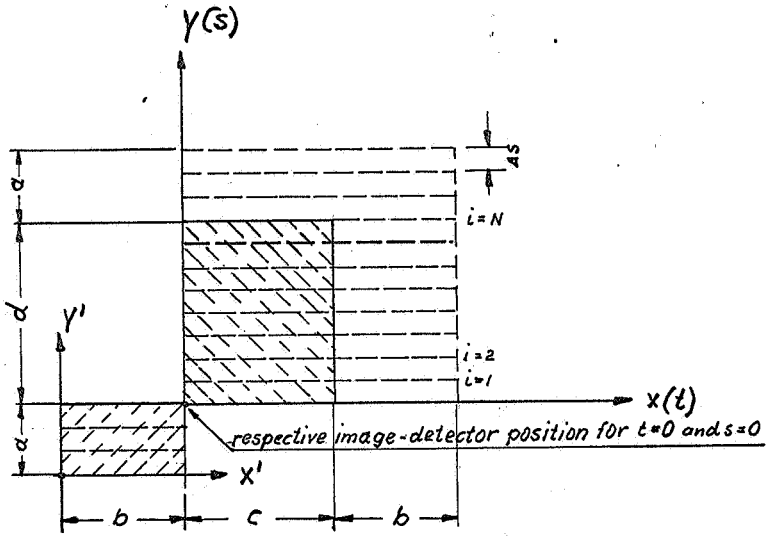

Fig. 6 Pattern of Scanning

To simplify the derivation we assume also that

$$b = N\Delta s$$

and $d = M\Delta s$, where N and M are integers.

Using figures 5 or 6 we get the relationships

$$x = t - a + x'$$

and $$y = i\Delta s - b + y'$$

The output of the detector due to an infinitesimal area dx dy is $A(x',y')\,B(x,y)\,dx\,dy$.

Integrating this signal during the scan we obtain in general

$$\int dt \int dy \int A(x',y')\,B(x,y)\,dx$$
$$= \int dt \int dy \int A(x+a-t, y+b-i\Delta s)\,B(x,y)\,dx .$$

Let us consider the case that $i < N$ which means that the beam is only partially incident on the detector at any position during the scan. For the first scan the integral becomes

$$I_1 = \int_0^{a+c} dt \int_{y=0}^{\Delta s} dy \int_{x=0}^{t} A(x+a-t, y+b-\Delta s)\,B(x,y)\,dx$$

For the second scan we get

$$I_2 = \int_0^{a+c} dt \int_0^{2\Delta s} dy \int_{x=0}^{t} A(x+a-t, y+b-2\Delta s)\,B(x,y)\,dx$$

or in general for $i < N$ we obtain

$$I_i = \int_0^{a+c} dt \int_0^{i\Delta s} dy \int_{x=0}^{t} A(x+a-t, y+b-i\Delta s)\,B(x,y)\,dx$$

where

$$i = 1, \cdots, N-1 .$$

Next we consider the case $N \le i \le M$, which means that the beam has been moved in y direction by a distance $\ge b$.

For this case the integral becomes

$$I_i = \int_0^{a+c} dt \int_{i\Delta s - b}^{i\Delta s} d\gamma \int_{x=0}^{t} A(x+a-t, \gamma+b-i\Delta s)\, B(x,\gamma)\, dx ,$$

where

$$i = N, \dots, M .$$

The last case is that for which $M \le i \le M+N-1$.

For the last case we get

$$I_i = \int_{t=0}^{a+c} dt \int_{\gamma=i\Delta s-b}^{d} d\gamma \int_{x=0}^{t} A(x+a-t, \gamma+b-i\Delta s)\, B(x,\gamma)\, dx .$$

Thus the recording of a total scan has the form

$$I = \sum_{i=1}^{N-1} \int_{t=0}^{a+c} dt \int_{\gamma=0}^{i\Delta s} d\gamma \int_{x=0}^{t} A(x+a-t, \gamma+b-i\Delta s)\, B(x,\gamma)\, dx +$$

$$+ \sum_{i=N}^{M} \int_{t=0}^{a+c} dt \int_{\gamma=i\Delta s-b}^{i\Delta s} d\gamma \int_{x=0}^{t} A(x+a-t, \gamma+b-i\Delta s)\, B(x,\gamma)\, dx +$$

$$+ \sum_{i=M+1}^{M+N-1} \int_{t=0}^{a+c} dt \int_{\gamma=i\Delta s-b}^{d} d\gamma \int_{x=0}^{t} A(x+a-t, \gamma+b-i\Delta s)\, B(x,\gamma)\, dx .$$

Now, we consider the first sum, namely

$$\sum_{i=1}^{N-1} \int_{t=0}^{a+c} dt \int_{\gamma=0}^{i\Delta s} d\gamma \int_{x=0}^{t} A(x+a-t, \gamma+b-i\Delta s) B(x,\gamma)\, dx .$$

Looking at Fig. 6 we see that the integration in x-direction has to be performed in three parts as follows

$$\sum_{i=1}^{N-1} \left\{ \int_{t=0}^{a} dt \int_{\gamma=0}^{i\Delta s} d\gamma \int_{x=0}^{t} A(x+a-t, \gamma+b-i\Delta s) B(x,\gamma)\, dx + \right.$$

$$+ \int_{t=a}^{c} dt \int_{\gamma=0}^{i\Delta s} d\gamma \int_{x=t-a}^{t} A(x+a-t, \gamma+b-i\Delta s) B(x,\gamma)\, dx +$$

$$\left. + \int_{c}^{c+a} dt \int_{\gamma=0}^{i\Delta s} d\gamma \int_{x=t-a}^{t} A(x+a-t, \gamma+b-i\Delta s) B(x,\gamma)\, dx \right\} .$$

This sum can be transformed in the following manner. First we change the order of integration and obtain

$$\sum_{i=1}^{N-1} \left\{ \int_{\gamma=0}^{i\Delta s} d\gamma \left[\int_{t=0}^{a} dt \int_{x=0}^{t} A(x+a-t, \gamma+b-i\Delta s) B(x,\gamma)\, dx + \right.\right.$$

$$\left.\left. + \int_{t=a}^{c} dt \int_{x=t-a}^{t} A(x+a-t, \gamma+b-i\Delta s) B(x,\gamma)\, dx + \right.\right.$$

$$+\int_{t=c}^{c+a} dt \int_{x=t-a}^{t} A(x+a-t,\gamma+b-i\Delta s)\,B(x,\gamma)\,dx\ .$$

As next we perform a linear transformation using the transformation equations

$$u = x+a-t$$

$$v = x\ .$$

With this and also transforming the limits of integration from the x,t - region into the v,u - region we get

$$\sum_{i=1}^{N-1}\left\{\int_{\gamma=0}^{i\Delta s} d\gamma\left[\int_{u=0}^{-a} du \int_{v=0}^{u} A(u,\gamma+b-i\Delta s)\,B(v,\gamma)\,dv + \right.\right.$$

$$+\int_{u=0}^{a} du \int_{v=u}^{u+c-a} A(u,\gamma+b-i\Delta s)\,B(v,\gamma)\,dv +$$

$$\left.\left. +\int_{u=0}^{a} du \left[\int_{v=u+c-a}^{c} A(u,\gamma+b-i\Delta s)\,B(v,\gamma)\,dv\right]\right\} =$$

$$= \sum_{i=1}^{N-1} \left\{ \int_{\gamma=0}^{i\Delta s} d\gamma \int_{u=0}^{a} du \left[\int_{v=0}^{u} A(u,\gamma+b-i\Delta s)\, B(v,\gamma)\, dv + \right.\right.$$

$$+ \int_{v=u}^{u+c-a} A(u,\gamma+b-i\Delta s)\, B(v,\gamma)\, dv +$$

$$\left.\left. + \int_{v=u+c-a}^{c} A(u,\gamma+b-i\Delta s)\, B(v,\gamma)\, dv \right] \right\} =$$

$$= \sum_{i=1}^{N-1} \int_{\gamma=0}^{i\Delta s} d\gamma \int_{u=0}^{a} du \int_{v=0}^{c} A(u,\gamma+b-i\Delta s)\, B(v,\gamma)\, dv =$$

$$= \sum_{i=1}^{N-1} \int_{\gamma=0}^{i\Delta s} d\gamma \left[\int_{0}^{a} A(u,\gamma+b-i\Delta s)\, d\gamma \int_{0}^{c} B(v,\gamma)\, dv \right].$$

If we define a quantity $\bar{B}(\gamma)$ and a quantity $\bar{A}(\gamma+b-i\Delta s)$ such that

$$\bar{B}(\gamma) = \int_{0}^{c} B(v,\gamma)\, dv \quad \text{and}$$

$$\bar{A}(\gamma+b-i\Delta s) = \int_{0}^{a} A(u,\gamma+b-i\Delta s)\, du$$

the sum becomes

$$\sum_{i=1}^{N-1} \int_{y=0}^{i\Delta s} \bar{B}(y)\bar{A}(y+b-i\Delta s)\,dy .$$

$\bar{B}(y)/c$ can be interpreted as the mean value of $B(x,y)$ averaged over x for a given y, where $0 \le x \le c$ and $\bar{A}(y+b-i\Delta s)/a$ can be regarded as the mean value of $A(x',y')$ averaged over x' where $0 \le x' \le a$ for a given y and during a given scan (scan with the index i).

Transforming the remaining sums in a similar manner we obtain for the total scan

$$I = \sum_{i=1}^{N-1} \int_{y=0}^{i\Delta s} \bar{B}(y)\bar{A}(y+b-i\Delta s)\,dy +$$

$$+ \sum_{i=N}^{M} \int_{y=0}^{i\Delta s} \bar{B}(y)\bar{A}(y+b-i\Delta s)\,dy +$$

$$+ \sum_{i=M+1}^{M+N-1} \int_{y=i\Delta s-b}^{d} \bar{B}(y)\bar{A}(y+b-i\Delta s)\,dy .$$

This situation can be illustrated as shown in Fig. 7

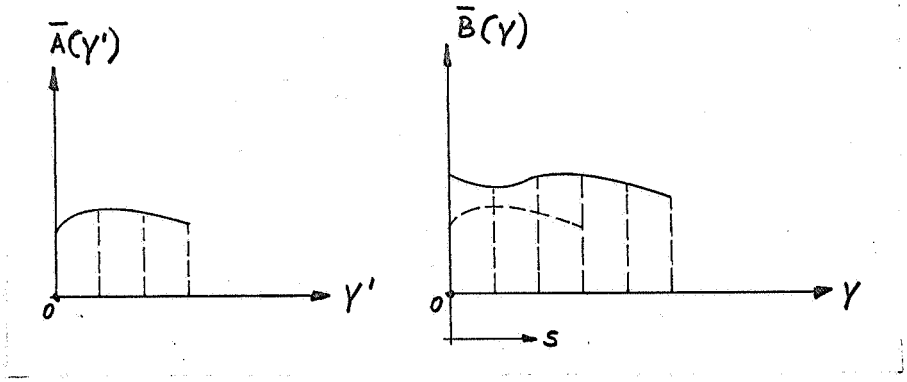

Fig. 7 Illustration to Detector Scanning

If we increase the number of scans Δs becomes smaller. Assume that the number of scans is increased to the extent that Δs approaches zero. If $\bar{B}(\gamma)$ and $\bar{A}(\gamma+b-i\Delta s)$ are continuous* functions the sum becomes a Rieman Integral or

$$I = \int_{s=0}^{b} ds \int_{\gamma=0}^{s} \bar{B}(\gamma)\bar{A}(\gamma+b-s)d\gamma + \int_{s=b}^{d} ds \int_{\gamma=s-b}^{s} \bar{B}(\gamma)\bar{A}(\gamma+b-s)d\gamma +$$

$$+ \int_{s=d}^{d+b} ds \int_{\gamma=s-b}^{d} \bar{B}(\gamma)\bar{A}(\gamma+b-s)d\gamma .$$

Again using a linear transformation of the form

$$w = \gamma + b - s$$

and $$z = \gamma$$

---

* This is a sufficient but not a necessary condition.

we obtain

$$I = \int_0^b \bar{A}(w)\left[\int_{z=0}^{w} \bar{B}(z)\,dz + \int_{z=w}^{w+d-b} \bar{B}(z)\,dz + \int_{z=w+d-b}^{d} \bar{B}(z)\,dz\right]dw$$

$$= \int_0^b \bar{A}(w)\left[\int_{z=0}^{d} \bar{B}(z)\,dz\right]dw = \int_0^b \bar{A}(w)\,dw \int_{z=0}^{d} \bar{B}(z)\,dz .$$

Substituting the definitions for $\bar{A}$ and $\bar{B}$ we finally arrive at

$$\bar{I} = \left[\int_0^b dy' \int_0^a A(x',y')\,dx'\right]\left[\int_0^d dy \int_0^c B(x,y)\,dx\right]$$

Since $A(x',y')$ is the flux density $\left[\text{WATTS}/\text{cm}^2\right]$ at the point (x',y') the integral

$$\int_0^b dy' \int_0^a A'(x',y')\,dx'$$

is the total flux passing through the image. The second integral could be interpreted as the output from the detector if a uniform flux with a flux density of $1\ \frac{\text{WATT}}{\text{cm}^2}$ would be incident on the detector. It is a detector constant. Therefore if we take the ratio of the integrated output of the scans of two beams through the same detector the second term drops out and we end up with the ratio of the fluxes contained in the two beams.

In reality it is of course impossible to use such a fine scan pattern that $\Delta S \to 0$. But we know that for any combination of functions, $A(x',y')$ and $B(x,y)$, there exists a ΔS small enough, that the value of the sum approaches the value of the integral with

any desired accuracy.

2.2.2 Experimental investigation of detector scanning*

Fig. 8 shows the physical arrangement which was used to generate the scans. A stepping motor which was reversed after a certain number of steps in each direction drove an indexing head on one axis, while a synchronous motor drove the head continuously in one direction on the other axis, yielding the two scan patterns illustrated in the same figure. The analysis of section 2.2.1 applies also to each of these patterns.

Fig. 9, a schematic diagram of the system, is mostly self-evident. The optical signal in Fig. 9 is the beam whose radiant flux is to be measured, and the integrator is a voltage integrator which integrates the output of the synchronous amplifier. The integrator is started when the scan is started and stopped when the scan is stopped. Tests were run on the various components of this system to determine the accuracy which it could yield if there was no error due to the finite size of the raster spacing and to determine which components would limit the accuracy. It was found that the predominant source of error was the lack of stability in the optical signal, which was produced by a Globar source. Fig. 10 shows the results of the Globar stability study.

Fig. 11 illustrates an actual comparison of the radiant power in two beams of different sizes. The scanning pattern is shown with the detector and the two beams drawn to scale superimposed on the pattern. In this particular case beam 1 was a focused, monochromatic beam measured at the focus, and beam 2 is the same beam, but measured at a point a few centimeters closer to the source. Thus the ratio of the two integrated signals should be equal to 1, whereas it was measured to be 0.992 ± 0.008 at the 95% confidence level. Looking at the relative sizes of the detector

* This work was done by Jon Geist at the National Bureau of Standards, Washington, D.C. (See reference no. 8).

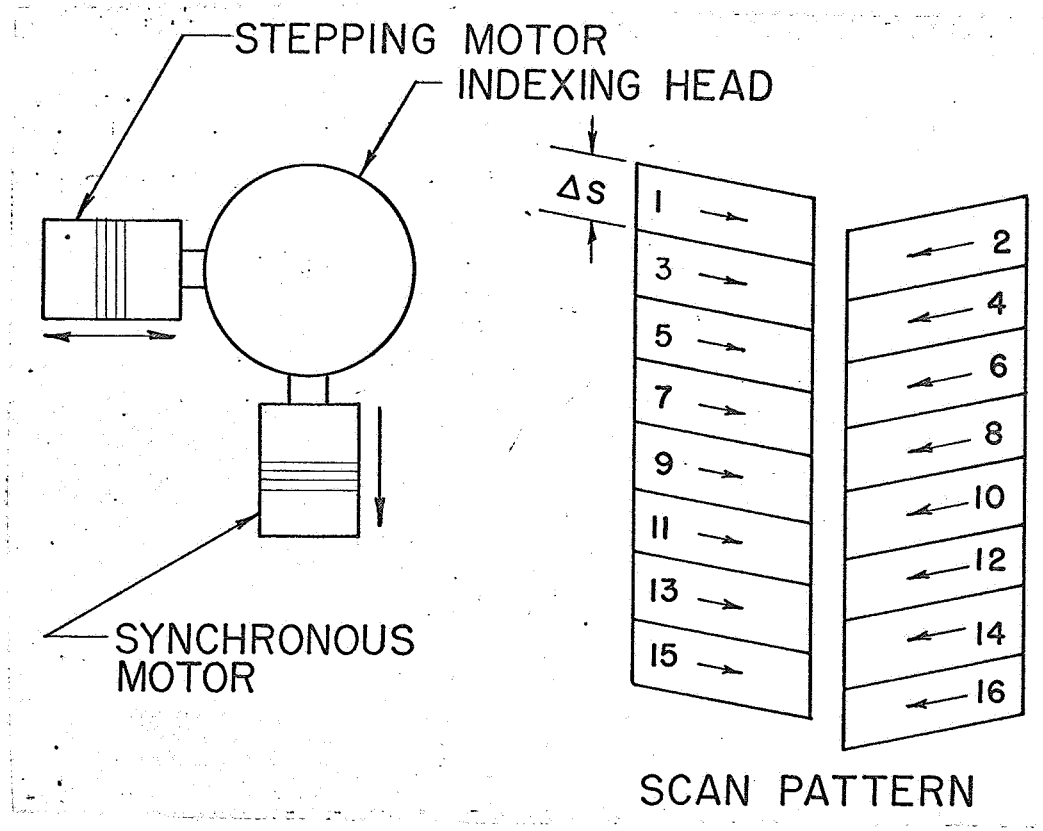

Fig. 8 Schematic of Scanning Mechanism

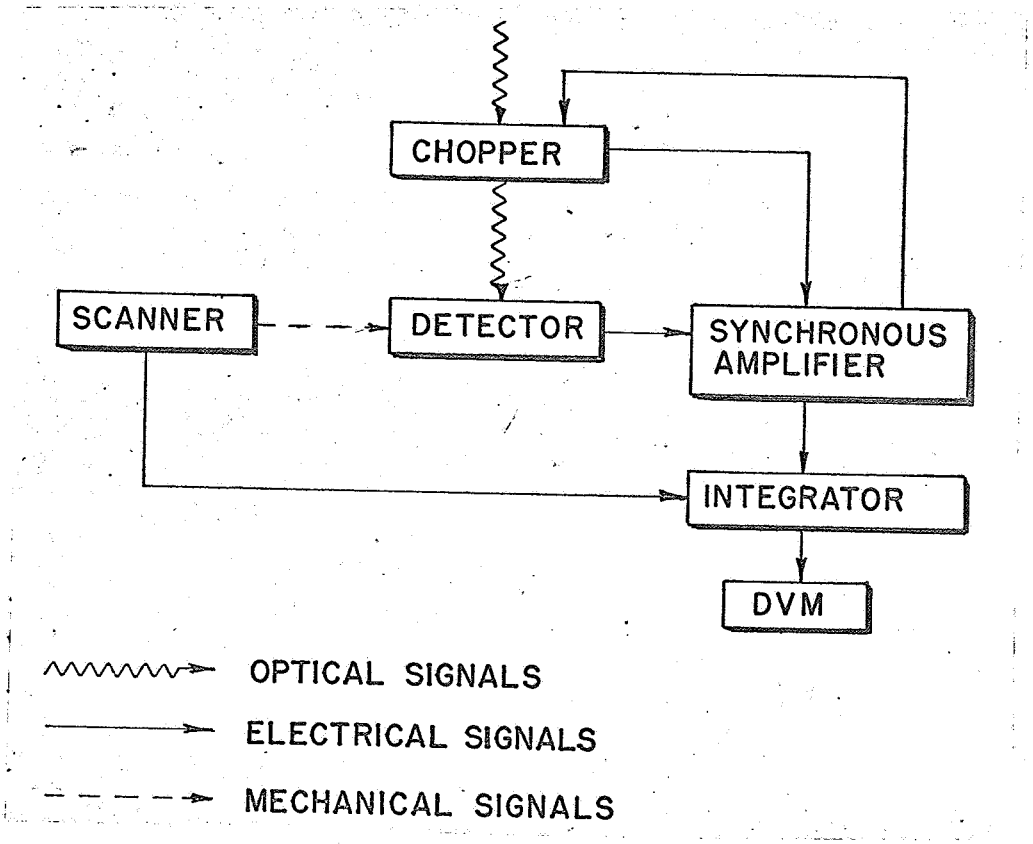

Fig. 9 Signal Flow Diagram

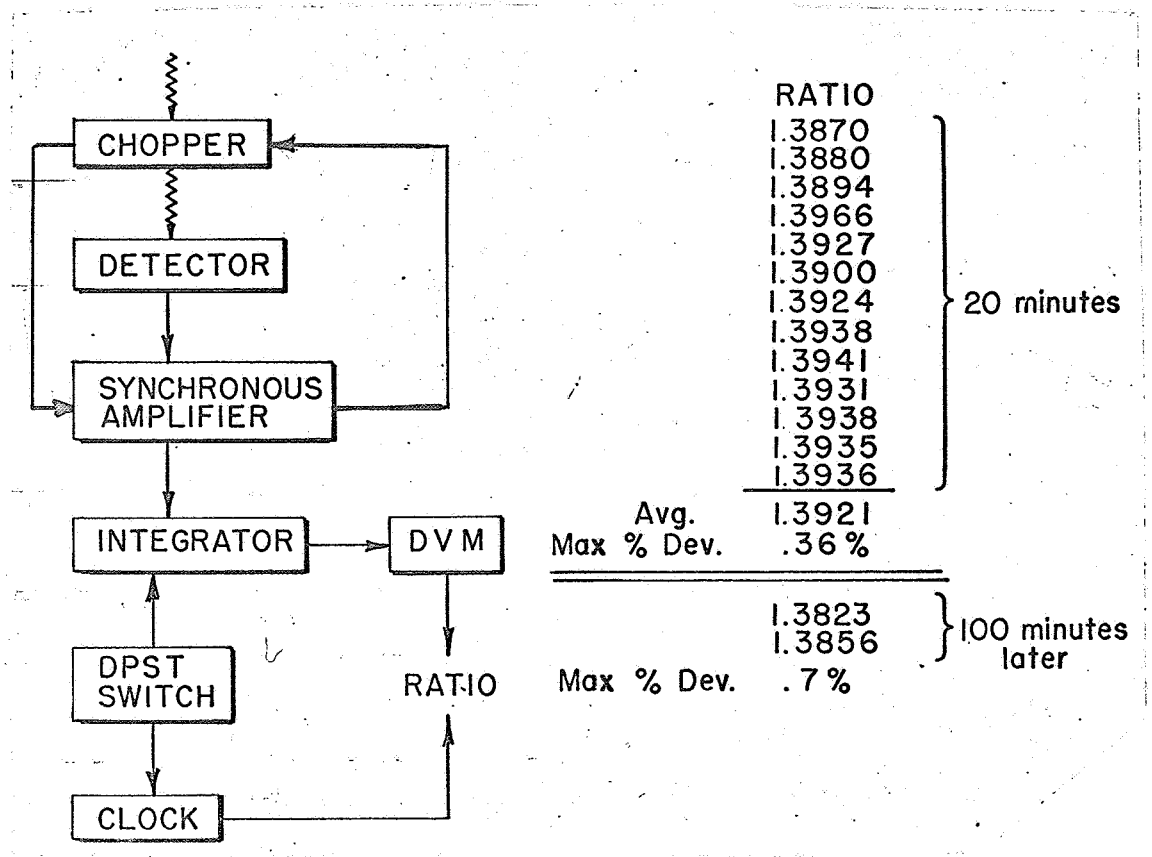

Fig. 10 Globar Stability Study

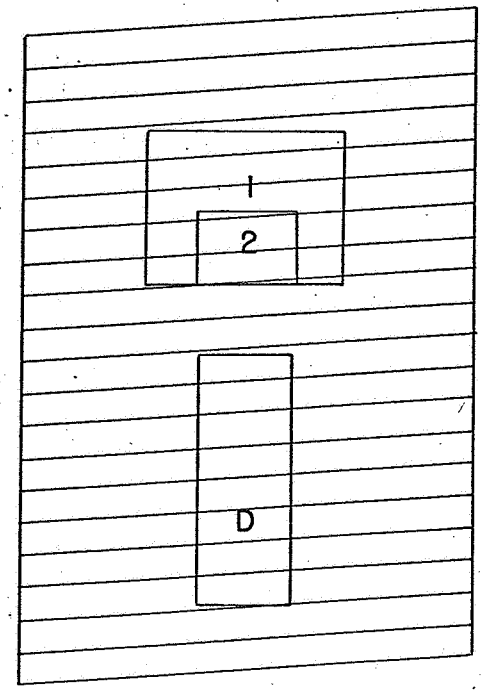

	1	2
	1.072	1.075
	1.064	1.084
	1.075	1.078
AVG.	1.0703	1.0790

Δ AVG = .0087 ± .0088

at 95 % level

Fig. 11 Comparison of Two Scans

and each beam, we see that a measurement of anywhere near this accuracy could not be done with this detector without using an averaging technique.

2.2.3 Efficiency of detector scanning.

We will have to use the following simplifying assumptions:

a) We assume that the responsivity is constant over the sensitive area of the detector.

b) The flux density is constant over the image.

c) We scan at a constant velocity v in x-direction, while the movement in y-direction by the distance ΔS occurs during a negligible time period.

Since for detector scanning the flux incident on the detector changes during the scan we will ask ourselves what is the average flux falling on the detector during one total scan.

The flux density within the image is ϕ_0 / A_I . The maximum flux incident on the detector during a total scan is therefore $\phi_0 (A_D / A_I)$.

Fig. 12 illustrates the flux incident on the detector, ϕ , as a function of x during one scan in x-direction.

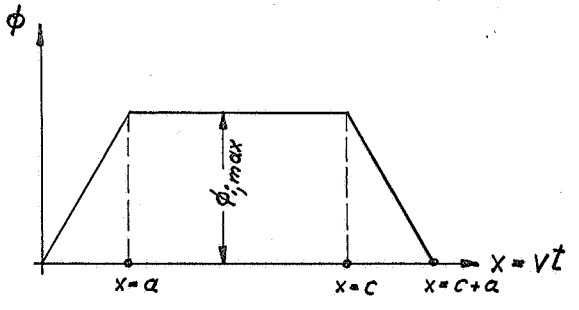

Fig. 12 The flux incident on the detector, ϕ , in x-direction for scan i.

The integrated flux is $c\,\phi_{i,\max}$. The time required for the scan is $(c+a)/V$. With this the time averaged flux during the scan i becomes

$$\bar{\phi}_i = \phi_{i,\max} \frac{cV}{c+a} .$$

$\phi_{i,\max}$ can be found as follows

For $i < N$ $\quad \phi_{i,\max} \simeq \phi_0 \frac{A_D}{A_I} \frac{i\Delta s}{N}$

For $N \leq i \leq M$ $\quad \phi_{i,\max} = \phi_0 \frac{A_D}{A_I}$

For $M < i \leq M+N-1$ $\quad \phi_{i,\max} = \phi_0 \frac{A_D}{A} \frac{i\Delta s}{N} (M+N-i)$.

Fig. 13 shows the signal as a function of time t for a total scan.

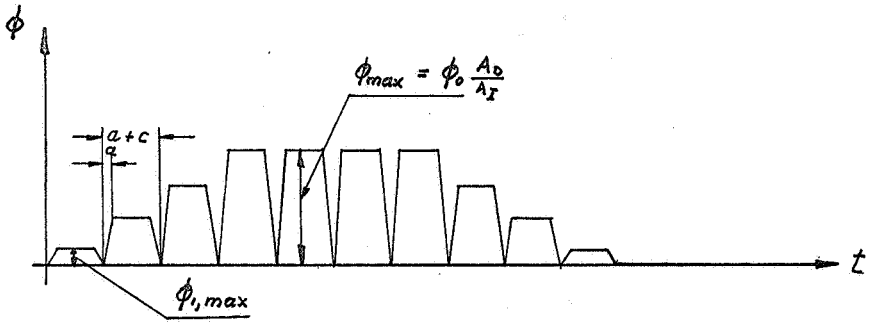

Fig. 13 Flux on the detector as a function of time, for a (N=4, M=7) total scan.

The number of scans required to complete a total scan is

$N + M = (b+d)/\Delta s$.

Therefore the total time required is $\left[(c+a)/v\right] \Big/ \left[(b+d)/\Delta s\right]$.

From Fig. 13 we see that the integrated flux is

$$\frac{c\,\phi_{max}}{c+a}\,\frac{M(c+a)}{v} = \phi_0 \frac{A_D}{A_I}\,\frac{cM}{v}\,.$$

The time averaged flux therefore becomes

$$\phi_0 \frac{A_D}{A_I}\,\frac{c}{v}\,\frac{M v \Delta s}{(c+a)(b+d)} = \phi_0 \frac{A_D}{A_I}\,\frac{cd}{(c+a)(b+d)}\,.$$

The average signal to noise ratio is found to be

$$\left(\frac{S}{N}\right)_2 = \phi_0 \frac{A_D}{A_I}\,\frac{cd\,D^*}{(c+a)(b+d)\sqrt{A_D \Delta f}}\,.$$

If the image is put directly on the detector the signal to noise ratio is, as was calculated earlier:

$$\left(\frac{S}{N}\right)_1 = \phi_0 \frac{A_D}{A_I}\,\frac{D^*}{\sqrt{A_D \Delta f}}$$

and the efficiency

$$\frac{(S/N)_2}{(S/N)_1} = \frac{cd}{(c+a)(b+d)}\,.$$

If we define two ratios α and β such that $\alpha = \frac{a}{c}$ and $\beta = \frac{b}{d}$ the efficiency becomes

$$\frac{1}{(1+\alpha)(1+\beta)}\,.$$

This result has been obtained assuming that $a \leq c$ and $b \leq d$. Without going through the derivation we will give the results for all four possible cases (assuming rectangular shape for the image as well as the detector), showing the relative size of detector and image. The symbol E_s is used for the efficiency of detector scanning.

Case 1:

$\alpha \geq 1$

$\beta \geq 1$

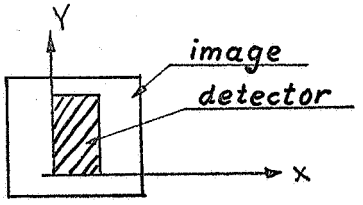

$$E_s = \frac{\alpha \beta}{(1+\alpha)(1+\beta)}$$

Case 2: $\alpha \geq 1$

$\beta \geq 1$

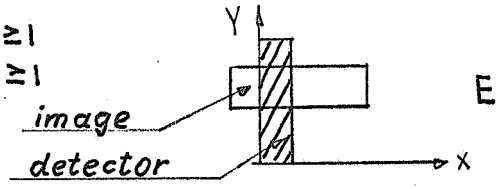

$$E_s = \frac{\alpha}{(1+\alpha)(1+\beta)}$$

Case 3: $\alpha \leq 1$

$\beta \geq 1$

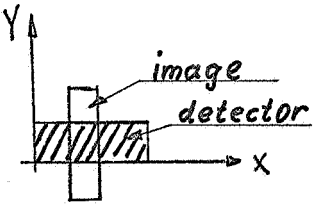

$$E_s = \frac{\beta}{(1+\alpha)(1+\beta)}$$

Case 4: $\alpha \leq 1$

$\beta \leq 1$

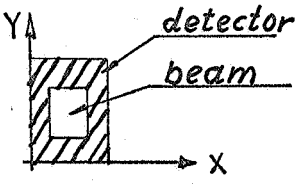

$$E_s = \frac{1}{(1+\alpha)(1+\beta)}$$

2.3 Comparison of the efficiency of averaging by an averaging sphere and by detector scanning.

2.3.1 Image and detector area are of the same size and shape.

In Section 2.1.2 the efficiency of averaging by a sphere, E_{sp}, was found to be

$$E_{sp} = A_I \frac{\rho_w^2}{A - \rho_w [A - (A_E + A_D)]}$$

To calculate the efficiency we have to assume some dimensions. We will approximately choose dimensions which would be used in an actual system.

Radius of averaging sphere, R, : R = 2.5 cm

$A = 4R^2\pi = 78.5\ cm^2$

A_I = 1.2 cm x 1.2 cm = 1.44 cm^2 (This corresponds to an image size at the first focal point of 0.2 cm x 0.2 cm.)

$A_E = (1.2)A_I = 1.73\ cm^2$ (This assures that all the flux is entering the sphere)

$A_D = A_I$

Using the dimensions above the efficiency becomes

$$E_{sp} = \frac{\rho_w^2}{54.5\,(1 - 0.96\rho_w)}$$

Since image and detector area have the same size and shape $\alpha = \beta = 1$ and the efficiency of detector scanning becomes simply

$$E_s = \frac{1}{(1+\alpha)(1+\beta)} = \frac{1}{4} = 0.25\ .$$

Using the expressions for E_{sp} and E_s we can calculate E_s/E_{sp} as a function of ρ_w . Fig.14 shows a plot of that function. Also included in Fig. 14 is the relative measurement time required for the averaging sphere to achieve the same signal to noise ratio as

detector scanning. This function is called τ_{sp}/τ_s . It is given by $\tau_{sp}/\tau_s = (E_s/E_{sp})^2$. As we can see from Fig. 14 detector scanning becomes more efficient when the reflectance of the sphere coating drops below 0.97. At a reflectance of 0.90 scanning gives a signal to noise ratio which is 2.3 times higher than that obtained with an averaging sphere. This means that using an averaging sphere one would have to increase the measurement time by a factor of 5.24 to obtain the same signal to noise ratio as with detector scanning.

2.3.2 Image size is the same as in Section 2.3.1 but in this case the detector has a sensitive area of 0.1 cm x 0.5 cm (c x d).

Using an A_D of 0.05 cm^2 we obtain for the sphere efficiency

$$E_{sp} = \frac{\rho_w^2}{54.5\,(1 - 0.978\rho_w)} \quad .$$

As we see there is only a slight change in the sphere efficiency. This might seem surprising since the flux incident on the detector is directly proportional to A_D, while the noise equivalent power (NEP) decreases only by the square root of A_D . Therefore the signal to noise ratio decreases proportional with the square root of A_D . But the same argument holds for a detector placed directly into the beam. Since the efficiency has been defined as the relative signal to noise ratio the decrease does not appear in the equation. Nevertheless it should be kept in mind that the absolute signal to noise ratio will decrease proportional to the square root of A_D .

The efficiency of detector scanning for $\alpha > 1$ and $\beta > 1$ has been calculated to be

$$E_s = \frac{\alpha\beta}{(1+\alpha)(1+\beta)} ,$$

where $\alpha = \frac{a}{c} = \frac{1.2}{0.1} = 12$ and

$$\beta = \frac{b}{d} = \frac{1.2}{0.5} = 2.4 \quad .$$

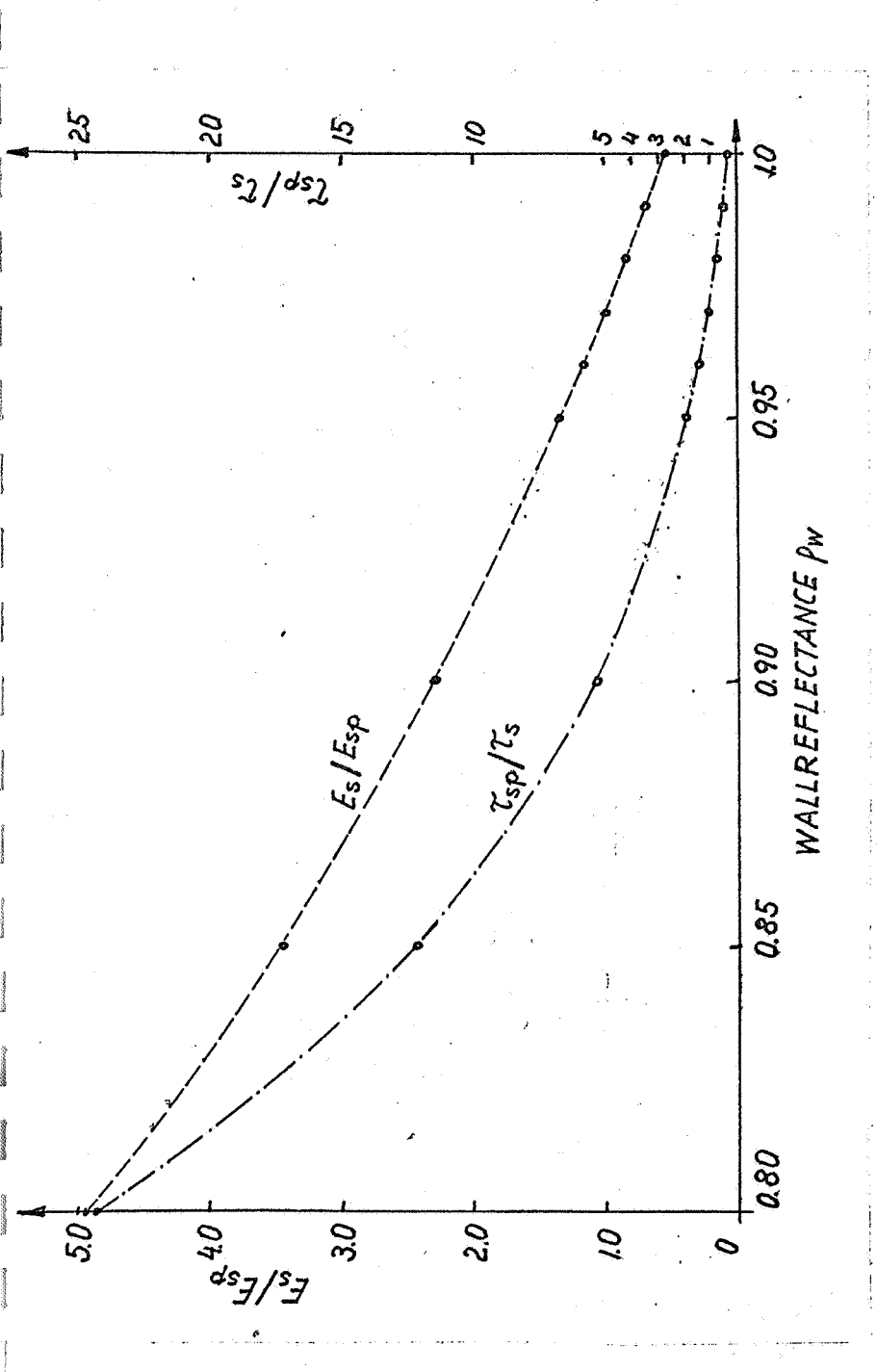

Fig. 14 Efficiency of detector scanning relative to the efficiency of averaging by a sphere.

With this E_s becomes

$$E = \frac{(12)(2.4)}{(13)(3.4)} = 0.652.$$

Fig. 15 gives the relative signal to noise ratio and relative measurement time for this case. From Fig. 15 we see that even with a sphere wall reflectance of 0.99 detector scanning is 1.16 times more efficient than averaging by a sphere. It shows that for small detectors scanning is a much better choice as far as signal to noise ratio is concerned.

Another question one might ask is, how do the scan times compare for the two cases investigated, assuming that the same spacing ΔS and the same scan velocity v is being used.

The time required for a total scan had been calculated as

$$[(c+a)/v]/[(b+d)/\Delta s] .$$

The ratio of the scanning times becomes

$$\frac{(c_1+a_1)(b_1+d_1)}{(c_2+a_2)(b_2+d_2)}$$, where

the index 1 refers to the case of Section 2.3.1 and index 2 to the case of Section 2.3.2. Using the dimensions assumed for the two cases the ratio becomes

$$\frac{(2.4)(2.4)}{(0.1+1.2)(0.5+1.2)} ,$$

which is equal to 2.61. In other words the time for a total scan using a detector and image of the same size and shape is 2.61 times longer than for the case of the small detector.

A look at the equation for scanning reveals that for a square image the efficiency of detector scanning is the same for both configurations shown in Fig. 16. The same is true for the total scanning time, again assuming that the step ΔS and the scanning velocity v is the same in both cases.

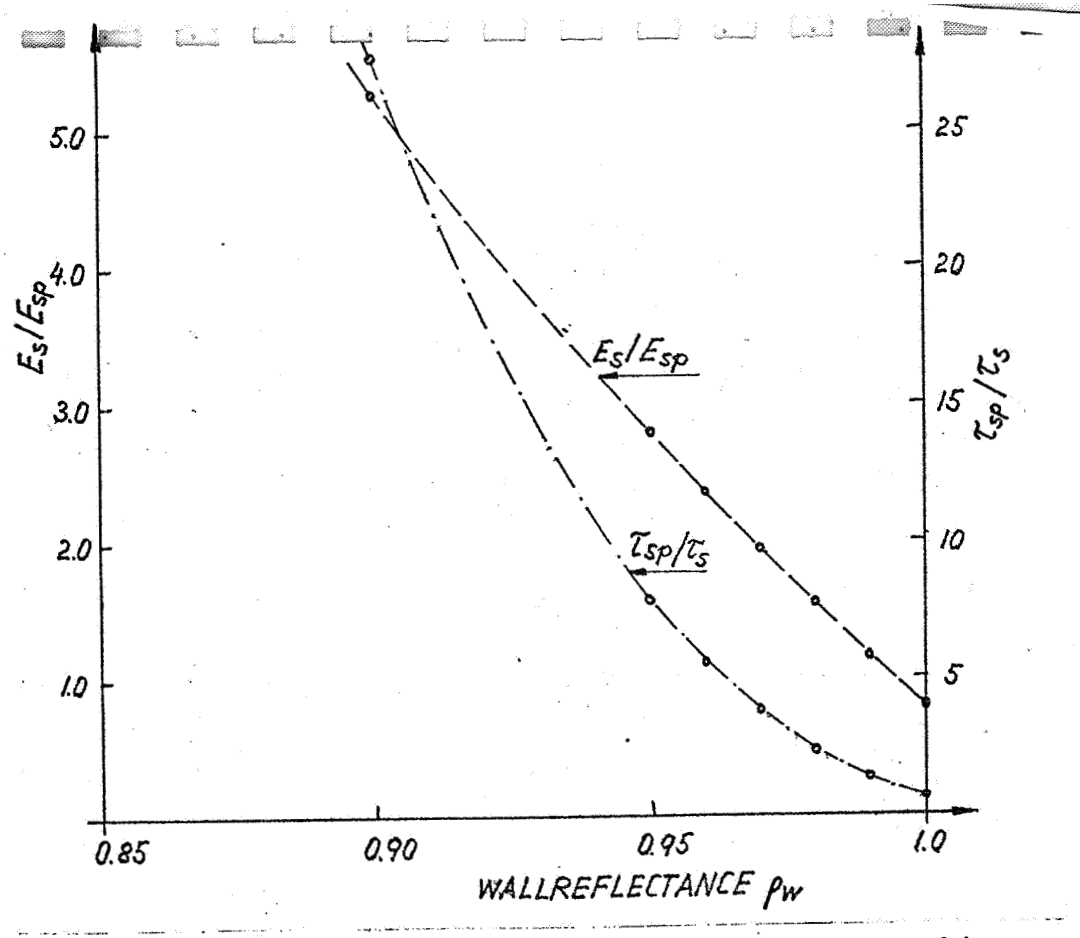

Fig. 15 Same as Fig. 14 for c = 0.1 cm and d = 0.5 cm ($\alpha = 12$; $\beta = 2.4$)

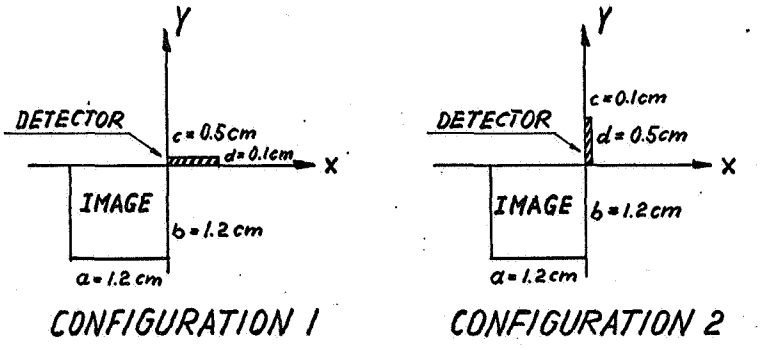

Fig. 16 Two scanning configurations

More image-detector configurations are of course possible but since the two cases investigated above are the most interesting for the EMR we will limit ourselves to the cases discussed in Sections 2.3.1 and 2.3.2.

2.4 Conclusions

From the foregoing discussion we can draw the following conclusions.

a) When large area detectors are available then averaging by a sphere is more efficient provided that a sphere coating of a very high reflectance is available. If the measurement allows, one might even want to sacrifice signal to noise ratio to take advantage of the simplicity of the averaging sphere. For our particular example if one can afford a decrease in signal to noise ratio by a factor of 2.3 the averaging sphere could be used over the wavelength range where the sphere coating has a reflectance of at least 0.9.

b) If the detector is small compared with the image, detector scanning becomes more efficient even at very high sphere coating reflectance. In our example of an image size of 1.2 cm x 1.2 cm and a detector size of 0.1 cm x 0.5 cm a drop in reflectance to 0.99 was enough to make detector scanning more efficient than the averaging sphere. A drop in reflectance to 0.90 showed scanning 5.26 times more efficient than using a sphere. Another way to look at this: If the reflectance of the sphere coating drops to 0.90, one would have to increase the measurement time by a factor of 27.67 to obtain the same signal to noise ratio as achieved by detector scanning.

3.0 Design study of a Fourier spectrometer - EMR system.

In the following sections we will study the components of the reflectometer and will make an attempt to find an optimum combination which will yield the highest possible signal to noise ratio over the wavelength region of interest.

3.1 The radiation source.

As a source of infrared radiation we will use a silicon carbide element (Globar) operated at 1400°K. We will treat the Globar as a blackbody radiator. Since the interferometer has a constant resolution if expressed in wavenumbers we will express the monochromatic flux as power per unit wavenumber interval emitted from a unit area into the halfspace. Fig. 17 shows a plot of the monochromatic flux of a 1400°K blackbody. The values were taken from radiation tables by Carmine C. Ferriso.[9] The monochromatic radiance $L_{\lambda,b}$ can be obtained from those values using the equation $L_{\lambda,b} = \phi_{\lambda,b} / \pi$. The flux passing through the image plane at the second focal point of the ellipsoidal mirror can be calculated as

$$\phi_\lambda = \rho_s \tau_{eff} A_I \Delta\nu \bar{\Omega} L_{\lambda,b}$$
$$= \frac{1}{\pi} \rho_s \tau_{eff} A_I \Delta\nu \bar{\Omega} \phi_{\lambda,b} ,$$

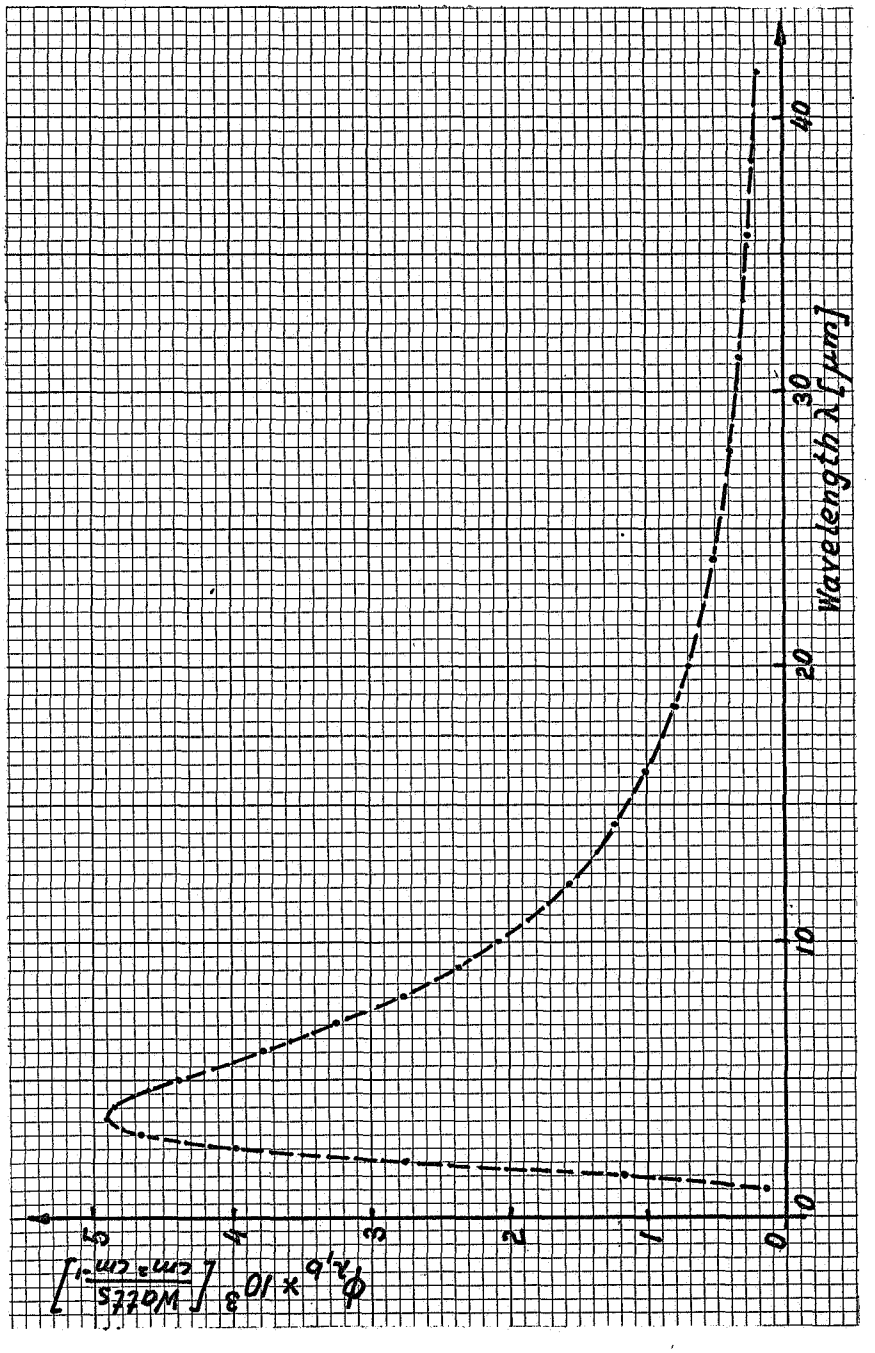

Fig. 17 Monochromatic flux from a 1400°K Blackbody

where ρ_s is the reflectance of the sample.

τ_{eff} the effective transmittance of the optical system from the Globar to the sample

A_I is the area of the image on the sample measured perpendicular to the incident beam. (if A_{ir} is the irradiated area of the sample then $A_I = A_{ir} / \cos\varphi$ with φ being the angle between the chief ray of the incident beam and the normal to the sample's surface).

$\Delta\nu$ is the spectral bandwidth of the instrument in cm^{-1}.

$\bar{\Omega}$ the weighted solid angle of the beam incident on the sample. (For a conical solid angle centered around the normal of a surface it is given by

$$\bar{\Omega} = \int_{\varphi=0}^{2\pi} \int_{\theta=0}^{\theta_1} \cos\theta \sin\theta \, d\theta \, d\varphi$$

$$= \pi \sin^2\theta_1 \quad , \text{ with } \theta_1 \text{ being the half angle of the cone).}$$

To make an estimate of the flux passing through the image at the second focal point (detectible flux we will have to assign values to the parameters defined above. Since $\bar{\Omega}$ and A_I determine the throughput of the system our first task will be to design the foreoptics and choose the size of the entrance port in the ellipsoidal mirror.

3.2 Foreoptics and size of entrance port.

The simplest way to bring the beam into the ellipsoidal mirror would be to focus the flux from the Globar through the interferometer onto the sample. This arrangement is shown in Fig. 18.

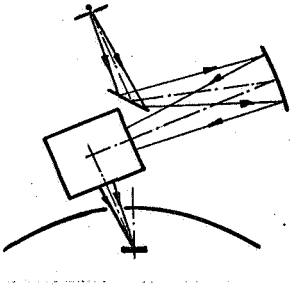

Fig. 18 Focusing through the interferometer

If we use the moving mirror of the interferometer as the limiting aperture, then the solid of the incident beam is given by the area of the moving mirror divided by the square of its distance from the sample. Using the actual dimensions of the interferometer and the ellipsoidal mirror the weighted solid angle, $\bar{\Omega}$, of the incident beam becomes 0.006 ster. If we further limit the image size at the second focal point to 12 cm x 1.2 cm the image at the first focal point has to be 0.2 cm x 0.2 cm = 0.04 cm^2. Using these values the throughput of the system becomes

$$0.04\ (0.006) = 2.4\ (10^{-4}) \left[\text{ster cm}^2\right].$$

Using the data supplied in the calibration report of Block Engineering, Inc., we find that the model 196TC interferometer (wavelength range 10 - 40μm) can handle a throughput of 5.67 x 10^{-2} cm^2 ster and that the model 196T (wavelength range 2 - 16μm) is capable of a throughput of 5.14 x 10^{-2} cm^2 ster. This shows that the throughput used by the foreoptics as discussed above is about 200 times less than the interferometer could use. Therefore we should look for an alternate and less wasteful approach. Fig. 19 gives an arrangement which, at least theoretically, could make full use of the throughput advantage of the interferometer. A water cooled diaphragm in front of the Globar has an aperture of about 0.2 x 0.2 cm^2. A spherical mirror produces a magnified image of the opening on the fixed mirror in the interferometer. The diverging beam which emerges from the interferometer is then condensed by another spherical mirror which produces an image of the diaphragm opening on the surface of the sample. The image on the sample has the dimensions of the original aperture. If one would magnify the image such that it would just fill the fixed mirror in the interferometer and would use a collecting mirror large enough to utilize the largest possible solid angle then the full throughput of the interferometer

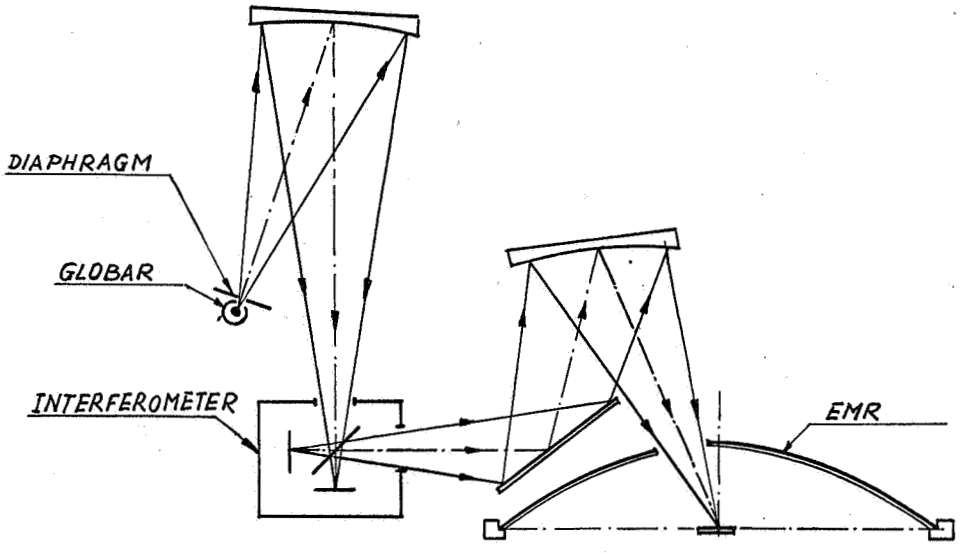

Fig. 19 Focusing onto the interferometer mirror

would have been realized. On the other hand a very large entrance port in the ellipsoidal mirror would be required because of large coneangle of the beam incident on the sample. This in return would cause a large entrance hole loss because part of the flux reflected by the sample would be lost out the entrance port and would, therefore, not reach the second focal point. This then leads to the question

of how much of a hole loss can be tolerated.

Our goal, as was stated in the introduction, was to design a reflectometer capable of measuring reflectance with an accuracy of 1% full scale. This could be achieved in two ways.

a) Every source of possible errors is designed in such a way that the sum of all errors becomes less than 1% or

b) one applies corrections for the errors such that the sum of the remaining errors becomes less than 1%.

Using the method mentioned under a) one trades accuracy for energy. Therefore in energy limited cases,as in ours, this is not a real possibility. For this reason we chose to correct the errors. This could be interpreted as a compromise between accuracy and convenience because each correction will require additional measurements. These additional measurements will be discussed in a later section. Having made the decision to use this approach we can now proceed with the design. As a starting point we limit the hole loss for a perfectly diffuse reflecting sample to 3% and calculate the coneangle for such a loss. The flux contained in a cone centered around the normal to the sample is given by

$$\Delta\phi_r = 2\pi \int_0^{\theta_1} L A_I \cos\theta \sin\theta \, d\theta$$

where L is the radiance of the reflected flux (constant for a perfect diffuser)

A_I is the irradiated area (dA is assumed small enough to consider the polar angle θ and the azimuthal angle φ essentially the same for any point within dA)

θ_1 is the half angle of the cone.

Since the total reflected flux, ϕ_r , for a perfect diffuser is $A_I \pi L$, the fraction of flux contained in the cone is given by

$$\frac{\Delta\phi_r}{\phi_r} = \frac{2\pi L A_I \int_0^{\theta_1} \cos\theta \sin\theta \, d\theta}{\pi L A_I}$$

$$= \sin^2 \theta_1 \, .$$

Using $\frac{\Delta\phi_r}{\phi_r} = 0.03$ we calculate θ_1 from $\sin\theta_1 = \sqrt{0.03} = 0.1732$ or $\theta_1 = 10°$. Since the throughput is equal to $dA\pi\sin^2\theta_1$ the throughput now becomes

$$TP = 0.04\pi\ 0.03 = 3.77 \times 10^{-3}\left[cm^2\ ster.\right]$$

This design therefore improves the utilization of throughput by a factor of $\frac{3.77 \times 10^{-3}}{2.4 \times 10^{-4}} = 15.7$, but we still use only about 7% of the maximum obtainable throughput.

The only parameters missing to calculate the flux passing through the image at the second focal point, ϕ_λ, are τ_{eff}, $\Delta\bar{\nu}$ and ρ_s. We assume a sample reflectance of 0.1 and an effective transmittance of 0.2 (this includes transmission losses through the interferometer and reflectance losses in the foreoptics). The spectral bandwidth of model 196T and 196TC Θ interferometer are given as 40 cm^{-1} and 20 cm^{-1} respectively. Using these values we calculate ϕ_λ as:

$$\phi_\lambda = \frac{\phi_{\lambda,b}}{\pi}\, 0.1(0.2)(3.8)(10^{-3})(40) \quad [WATTS]$$

$$= 0.97 \times 10^{-3}\,\phi_{\lambda,b} \approx 1 \times 10^{-3}\,\phi_{\lambda,b} \text{ for model 196T}$$

and $$\phi_\lambda \approx 0.5 \times 10^{-3}\,\phi_{\lambda,b}\ [WATTS] \text{ for model 196TC}$$

Fig. 20 and Fig. 21 show ϕ_λ for model 196T and model 196TC respectively.

Our next step will be to calculate the signal to noise ratio obtainable with the flux ϕ_λ. This cannot be done without selecting a specific detector. In the next section therefore we will consider a variety of detectors which could be used with the interferometers. From these detectors we will then choose the best suitable one and calculate the signal to noise ratio.

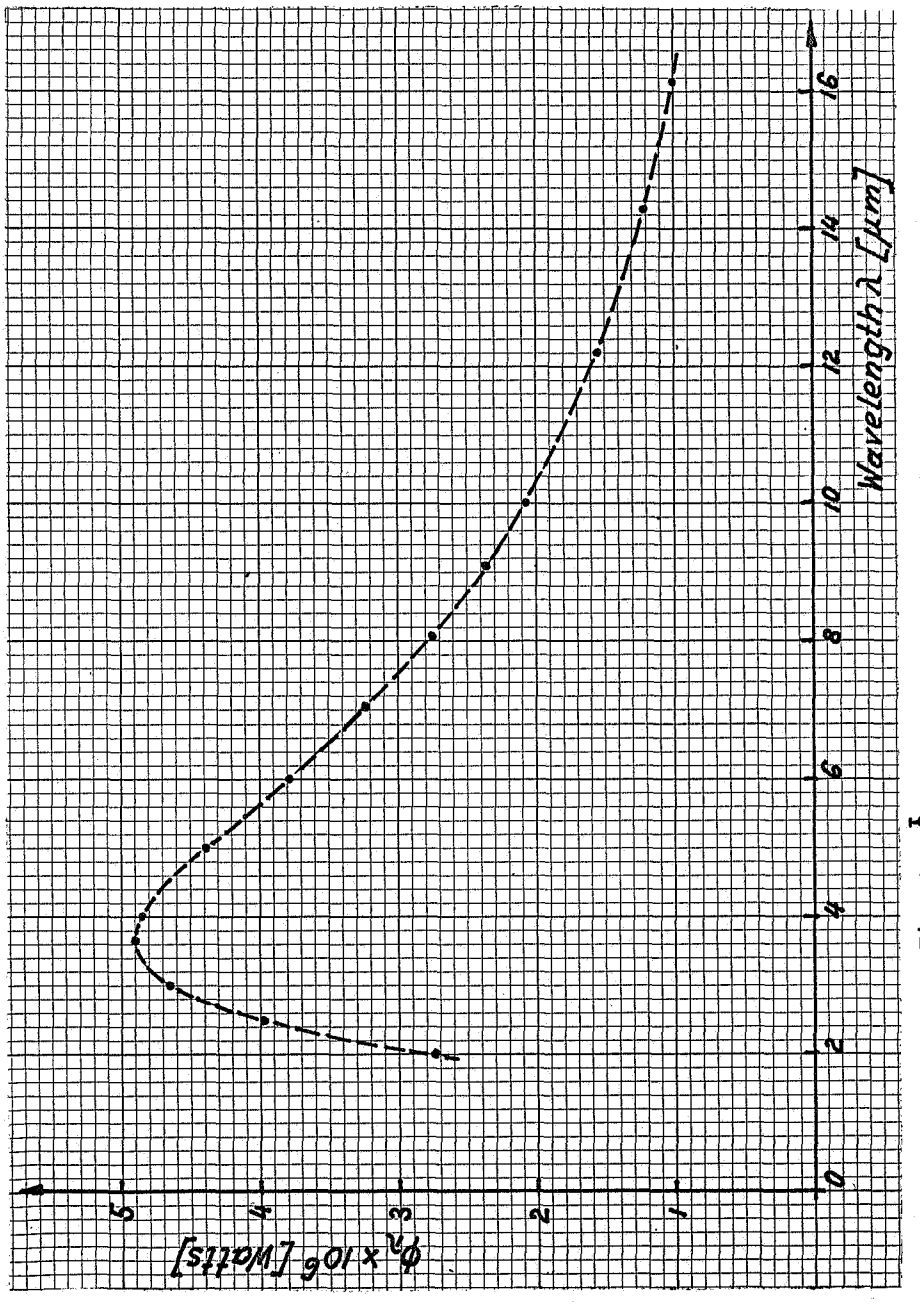

Fig. 20 $\Phi\lambda$ using model 196T interferometer

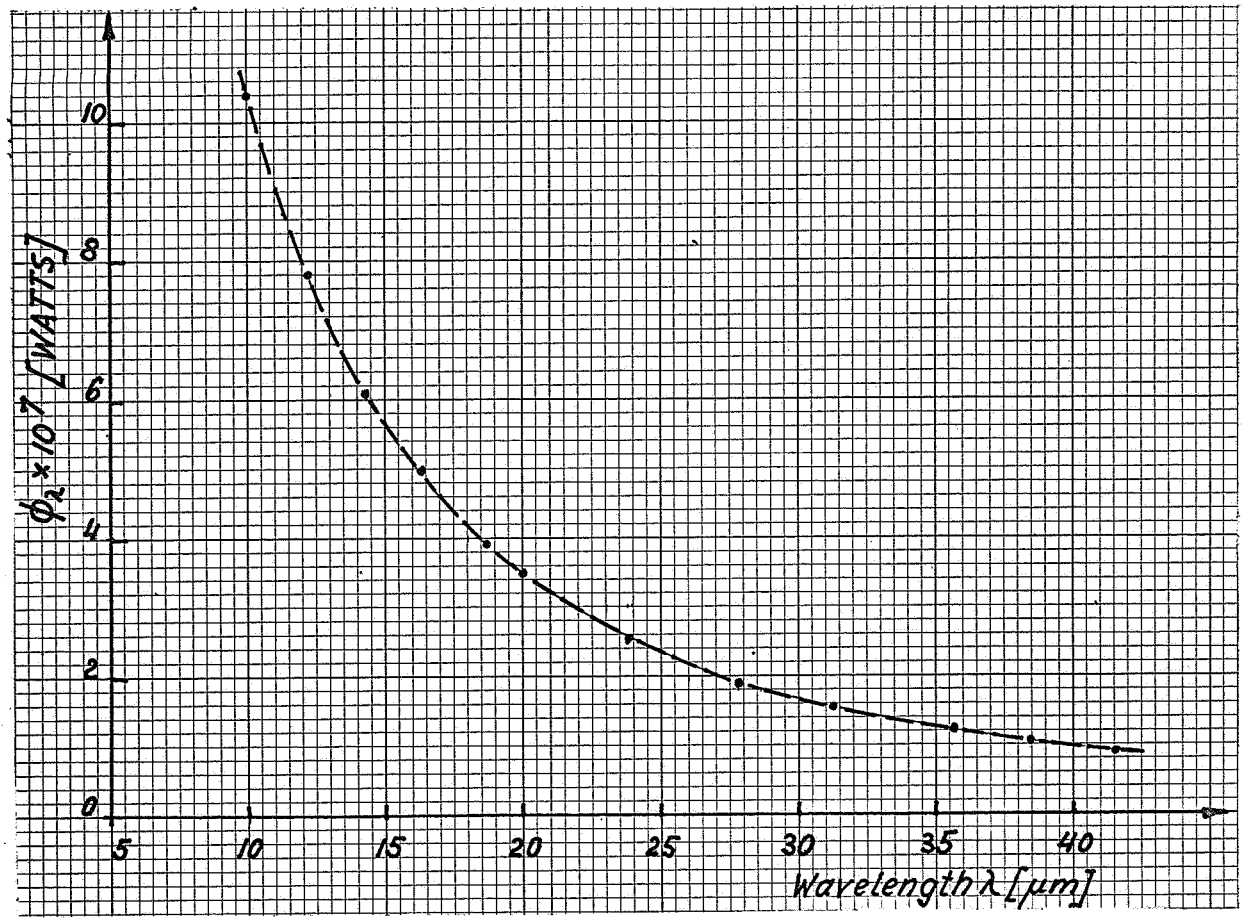

Fig. 21 Φ_λ using model 196TC interferometer

3.3 Detectors

Normally infrared detectors are divided into two groups, thermal detectors and photon detectors. For our case we will divide the detectors according to convenience. In the first group we will consider detectors which can be used at room temperature and in the second group we will discuss detectors which require cooling.

The parameters* which will be discussed will include:

a) the spectral detectivity (D*).

b) the time constant which describes the frequency variation of the detectivity or signal to noise ratio of the detector.

c) the variation of responsivity over the sensitive area of the detector.

d) the angular variation of responsivity.

e) available sizes of the detector.

3.3.1 Room temperature detectors.

Since the purpose of this investigation was the design of a Fourier spectrometer-EMR system we will only discuss those detectors which show at least some promise of success.

3.3.1.1 The Lead Selenide (Pb Se) cell

The Pb Se cell is a photoconductive detector. At room temperature it can be used over the wavelength range from 1 to 4μm. (This of course would limit its use for only a portion of the wavelength range of the model 196T Fourier spectrometer.) It is commercially available in various sizes up to 1cm x 1cm. Fig. 22 shows the range of D* (λ, 780) as taken from reference 12.

---

*The definition of these parameters can be found in references 10 and 11.

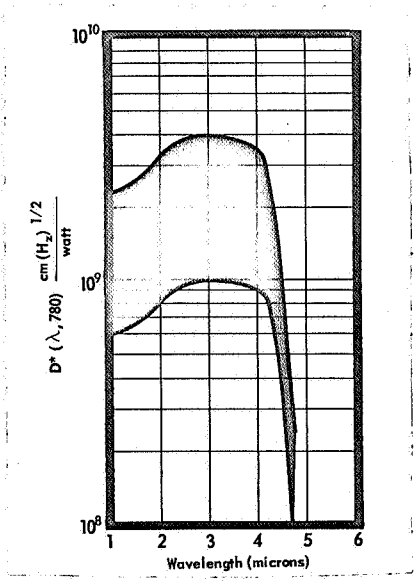

Fig. 22. Range of Spectral Detectivities for Ambient Pb Se Detectors at 295°K.

Reference 12 also indicates that the peak detectivity for elements less than 3mm x 3mm is greater than or equal to 1×10^9 $\left[cm\ (cps)^{\frac{1}{2}}/Watt\right]$. For elements larger than 3mm x 3mm the peak detectivity becomes smaller and is greater or equal to 6×10^8 $\left[cm\ (cps)^{\frac{1}{2}}/Watt\right]$. Since D* is the area normalized detectivity, it should be independent of detector area. But due to the fabrication process it is difficult to maintain the same average detectivity for large area detectors as for small area detectors. Therefore D* decreases with increasing detector area.

The time constant is given as $\leq$ 2 microseconds and the peak responsivity for a detector area of $1cm^2$ is between 1×10^2 and 6×10^6 $\left[Volts/Watt\right]$.

A lead selenide cell exhibits large variations of responsivity over its sensitive area. Some averaging technique is therefore necessary. Fig. 23, taken from reference 11, shows a "contour map" of a typical lead selenide cell. No data could be found on angular variation of responsivity.

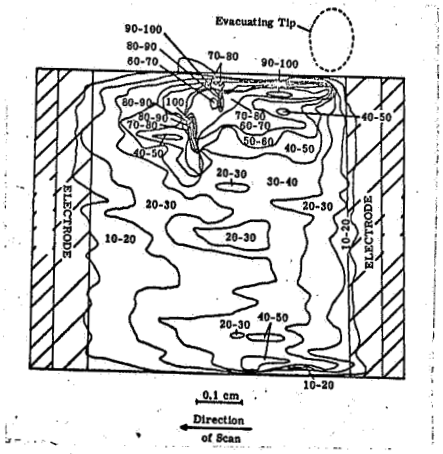

Fig. 23. Sensitivity contour for a typical Pb Se cell.

3.3.1.2. Indium antimonide (In Sb) photoconductive cell.

The room temperature In Sb cell is operated in the photoconductive mode. The wavelength range is about 2 to 7μm if we use the wavelengths where D* has dropped to half of its peak value as cut off points. The cell is available in sizes from (0.05 x 0.05)cm^2 to (0.2 x 0.5)cm^2. The time constant is given as less than 0.2 μ sec. Figures 24, 25 and 26 show parameters of a typical cell.*

*These figures were taken from a brochure "Infrared Detectors" by Mullard Limited, London.

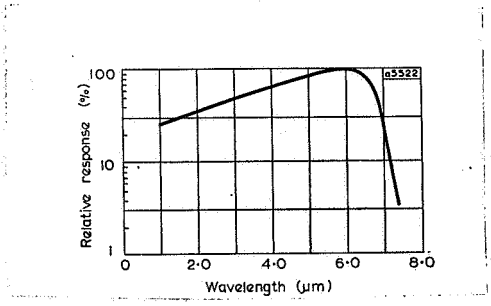

Fig. 24 Relative, spectral responsivity of a typical room temperature In Sb cell

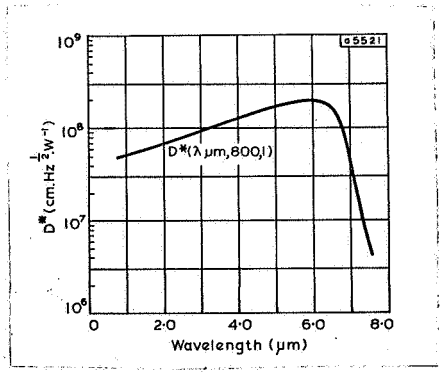

Fig. 25 D* (λ, 800,1) for a typical room temperature In Sb cell.

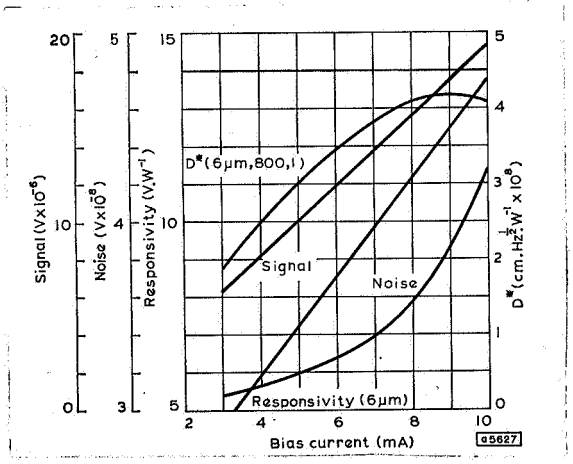

Fig. 26 Signal, noise, responsivity, and peak detectivity as a function of bias current for a typical room temperature In Sb cell.

3.3.1.3 Large area thermopile

The receiving element of these detectors is a gold-black coated gold foil. They have been manufactured in sizes up to (1.2 x 1.2) cm^2. The spectral responsivity of the thermopiles is determined by the absorptance of the gold-black coating and the transmittance of the window. The responsivity* is given as 2 volts/watt for unmodulated radiation. The time constant for a large area thermopile is about 40 milliseconds. The relatively long time constant is the main limitation of this detector for our application. It means that the detector reaches only 63% of its DC responsivity at a chopping frequency of 25 cps and only 10% at about 100 cps. The limiting noise is about equal to the Johnson noise and is given between 0.7 to 1 x 10^{-9} volts rms for a resistance of about 30 ohms.

Although the gold-black coating can have quite a uniform absorptance the thermopile still exhibits a large variation of sensitivity over its receiving area. Measurements of sensitivity variations have been made by Stair[13] et al. at NBS. The measurements showed that the sensitivity peaked at the locations of the junctions and dropped almost to zero in areas between the junctions. Therefore the thermopile could not be used without an averaging device.

At this point it seems worth while to inject a general comment about thermal detectors. The responsivity of a thermal detector is proportional to the thermal impedance of the detector. On the other hand the time constant increases proportionaly with increasing thermal impedance. The design of a particular thermal detector therefore requires a trade off of responsivity versus the time constant. As an example, from reference 14 (page 136) we find that the AC responsivity, defined as the ratio of the amplitude of the open-circuit voltage generated to the amplitude of the incident power, of a thermocouple,

---

*This information was taken from the thermopile catalogue of the Charles M. Reeder & Co., Inc., Detroit.

can be written as

$$\frac{V}{P} = \frac{SR}{[1 + \omega^2 (RC)^2]^{\frac{1}{2}}},$$

where S is the thermoelectric power of the material used,

R is the thermal impedance of the detector

C is the thermal capacitance of the detector

and W is the angular frequency of the modulated radiation.

At the present the Reeder Company is developing a LN_2 - cooled large area thermopile. Although not evident from the equation above, a higher responsivity and a smaller time constant is predicted. Dunn Associates has ordered the first two models and will test them with the Fourier spectrometer as soon as they will be delivered. Unfortunately the development of the cooled thermopile is much behind schedule.

3.3.1.4 Solid-Backed Evaporated Thermopile Radiation Detector.

This detector has been described in detail by Astheimer and Weiner.[15] It is formed by evaporating two metals, such as bismuth and antimony, onto a substrate through appropriate masks. In this way many junctions can be formed in almost any configuration. The responsivity is proportional to the number of junctions per unit area, but on the other hand the electrical resistivity increases also, which is accompanied by an increase in noise. According to reference 15 the main advantage the evaporated thermopile has over the Schwarz-type thermopile is its ruggedness. Table 1, taken from reference 15, compares the evaporated thermopile with a Schwarz-type thermocouple and a thermistor bolometer. As we can see from that table, a Schwarz-type thermocouple offers lower noise-equivalent-power and higher responsivity, while the evaporated thermopile has a faster time response. But as we have seen before, a faster time constant can always be achieved at the expense of responsivity. A more recent publication[16] of Barnes

Table I. Comparison of Long-Wavelength Detector Characteristics

Detector type	Receiver dimensions (mm)	Number of elements	DC responsivity $\mathcal{R}'$ (VW^{-1}/cm^2)	DC responsivity $\mathcal{R}$ (V/W)	τ (msec)	Resistance (Ω)	NEP (W)	D* 300°K, dc, 1 cps (cm/W)
Evaporated thermopile	1 × 8	40	0.02	0.25	8	30	2.8×10^{-9}	1×10^{8}
Evaporated thermopile	1 × 8	120	0.03	0.37	6	100	3.5×10^{-9}	0.8×10^{8}
Evaporated thermopile	2.5 diam	20	0.06	1.2	30	50	7.6×10^{-10}	3×10^{8}
Evaporated multiple layer thermopile	2.5 diam	40	0.12	2.4	40	150	6.6×10^{-10}	3.4×10^{8}
Schwarz-type thermocouple	2 × 2	1	0.20	5.0	35	10	8.2×10^{-11}	24×10^{8}
Thermistor bolometer	1 × 1	1	14.0	1400	15	2.3M	2×10^{-10}	5×10^{8}

Engineering gives a table with the characteristics of standard evaporated thermopiles. This table is shown as Table 2. The D* values, which do not include window losses, are lower than those given in Table 1.

3.3.1.5 The Thermistor bolometer*

The sensing element of a thermistor bolometer is a thermally sensitive resistor which undergoes a large change in resistance when exposed to radiation. The semiconductor flakes used by Barnes Engineering change their resistance by about four percent per degree K of temperature variation. The surface of the flake is blackened to increase the absorptance over a large wavelength region.

The temperature coefficient of resistance for a thermistor material is negative. This limits the bias voltage to a value which keeps Joule's heating to a minimum. Figure 27 shows the relationship between bias voltage and detector current for several detector resistances. To safeguard against detector "burnout" the reference mentioned

*Most of the information and figures presented are taken from "Thermistor Infrared Detectors", Bulletin 2-100 of Barnes Engineering Co., Stamford, Connecticut.

Type	2-212		2-214		2-215		Units
Target Dimensions	2.5 diameter		1 x 8		4.67 x 5.59		mm
Target Area	5		8		26.1		mm^2
Number of Junctions	20		120		308		---
Operating Temp.	-60 to +125		-60 to +125		-60 to +125		°C
Resistance	200		1000		5000		ohms
Environment	Atmosphere	Vacuum	Atmosphere	Vacuum	Atmosphere	Vacuum	
DC Responsivity (Notes 1 and 2)	1.4	2.4	0.62	1.0	0.69	1.1	volts/watt
	0.07	0.12	0.05	0.08	0.18	0.3	$\frac{\text{volts}}{\text{watt/cm}^2}$
Time Constant	200	400	15	25	18	30	milliseconds
Noise Equivalent Power	1.3×10^{-9}	0.8×10^{-9}	6.8×10^{-9}	4.2×10^{-9}	13×10^{-9}	8.1×10^{-9}	watts
D* (500°K, DC, 1) (Note 2)	1.7×10^{9}	2.9×10^{9}	0.4×10^{8}	0.6×10^{8}	0.4×10^{8}	0.6×10^{8}	$\text{cm-cps}^{1/2}\,\text{watt}^{-1}$

Note 1: Based on total irradiated area including spaces between junctions.

Note 2: Does not include window losses.

Table 2. Evaporated Thermopile Characteristics

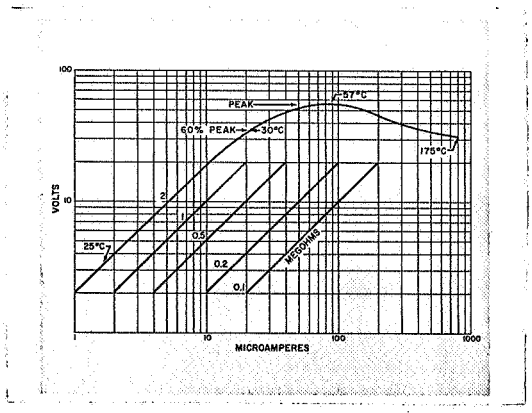

Fig. 27
Bias voltage - detector current relationship for thermistor bolometers

above recommends to operate the detector at 60% of its peak bias voltage.

As already discussed in connection with the thermopile, responsivity of a thermal detector can be traded against time constant. Figure 28 shows to what degree responsivity and time constant can be traded.

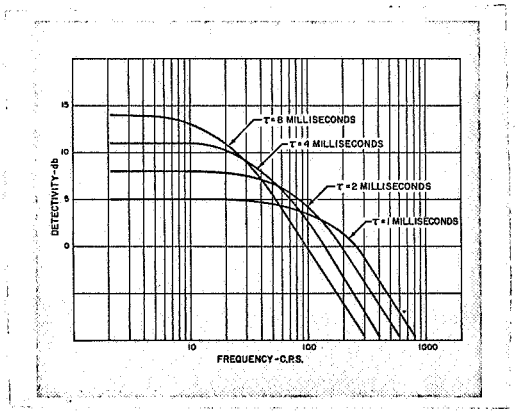

Fig. 28
Frequency-Response characteristics for thermistor bolometers

Reference 11 gives the following relationship between D* and the time constant:

$$D^* = 8 \times 10^9 \times \tau^{\frac{1}{2}}, \text{ where } \tau \text{ is in seconds.}$$

The limiting noise for thermistor bolometers is Johnson noise for modulation frequencies larger than about 40 cps and 1/f noise for frequencies less than or equal to 40 cps. Figure 29, taken from reference 11, shows D* as a function of modulation frequency.

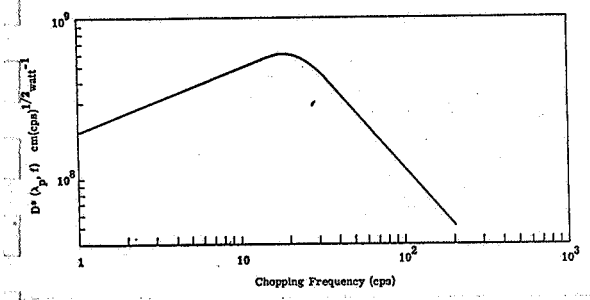

Fig. 29. $D^*(\lambda_p, f)$ as a function of modulation frequencies.

The time constant of commercially available detectors ranges from 0.8 to 8 milliseconds. The size of the flake ranges from $(0.03 \times 0.03)\text{cm}^2$ to $(0.25 \times 0.25)\text{cm}^2$.

Table 3 shows characteristics of thermistor bolometers available from the Barnes Engineering Company.

Table 3 Characteristics of commercially available thermistor bolometers

SOLID-BACKED THERMISTOR INFRARED DETECTORS (Flanged Base, No. 1 Thermistor Material)

Code No.	Sensitive Area (millimeters)	Time Constant (milliseconds)	Window Material (0.04" thick)	Resistance (megohms at 25°C)	Responsivity (Note 2) (volts/watt)
2-101	0.3 x 0.3	1.1	KRS-5	2.5	1065
2-102	0.3 x 0.3	2.5	KRS-5	2.5	1600
2-103	0.5 x 0.5	1.1	KRS-5	2.5	560
2-104	0.5 x 0.5	2.5	KRS-5	2.5	920
2-105	1.0 x 1.0	1.1	KRS-5	2.5	220
2-106	1.0 x 1.0	2.5	KRS-5	2.5	410
2-107	1.5 x 1.5	1.1	KRS-5	2.5	115
2-108	1.5 x 1.5	2.5	KRS-5	2.5	230
2-109	2.0 x 2.0	1.1	KRS-5	2.5	80
2-110	2.0 x 2.0	2.5	KRS-5	2.5	160
2-111	2.5 x 2.5	1.1	KRS-5	2.5	40
2-112	2.5 x 2.5	2.5	KRS-5	2.5	100

Note 2: Responsivity of solid-backed thermistor detectors is measured with KRS-5 window in place. Radiation is supplied by a blackbody at 470°K, mechanically chopped at 15 cps to produce a square-wave (50% duty cycle) radiation signal. Peak-to-peak input irradiance in the plane of the detector is 2.28 microwatts/mm^2. Listed responsivity is that of the active flake; in a bridge circuit responsivity is one-half this value.

The main handicap of this detector for our applications is its small size which, regardless of the presence of spatial variations of responsivity, would require image scanning.

3.3.1.6 The Pyroelectric Detector

This detector has been described by Astheimer[17] and Beerman[18] of Barnes Engineering Company. The following information is taken from references 17 and 18.

The heart of a pyroelectric detector is a piezoelectric crystal which also exhibits spontaneous polarization. These crystals are

called pyroelectric, since the value of spontaneous polarization is temperature dependent and a change in charge (and therefore voltage) will appear whenever the temperature is changed. The following equations, taken from reference 17, show the relationship between the responsivity of the detector and its physical parameters. R_o is the DC responsivity while R_ω is the responsivity at a modulation frequency ω.

$$R_o = \frac{\Omega A Z}{C} \sim \left(\frac{\Omega}{e}\right) \gamma Z$$

$$\tau = HZ = (h A \gamma) Z$$

$$R_\omega = \frac{R_o}{1 + i\omega\tau}$$

where: τ is the thermal time constant (sec)

Ω is the pyroelectric coefficient $\left[\text{coulombs}/^\circ\text{K-cm}^2\right] = dP_s/dt$ (the change in spontaneous polarization with temperature)

A is the area of the detector $\left[\text{cm}^2\right]$

Z is the thermal impedance $\left[^\circ\text{C/Watt}\right]$

e is the dielectric constant

γ is the thickness of the detector flake

c is the capacitance $\left[\text{farad}\right]$

The DC responsivity is proportional to Ω/e, which is a material constant and can be considered a figure of merit of the pyroelectric material. This figure is given as 4×10^{-10} $\left[\text{coulombs}/^\circ\text{C-cm}^2\right]$ for triglycine sulfate, the material used in the first commercial detectors. The equations also show that a thick flake would be desirable for a high DC responsivity which would however result in a slow thermal time constant. As shown in reference 17 a thin flake should be used to keep detector noise low.

The detector is normally used at frequencies above the thermal time constant. Besides the thermal time constant we have to consider an

electrical time constant which is determined by the capacitance of the detector and the input resistance of the amplifier. The electrical cut-off frequency is generally higher than the thermal cut-off frequency. The detector is normally operated between those two frequencies.

Since the pyroelectric detector is a pure capacitance it does not show "Johnson" noise and the limiting detector noise should be temperature noise, which is caused by random fluctuation of the temperature of the absorbing element. So far this limit has not been reached because the noise level of the amplifier was higher than the thermal noise of the detectors. The practical limiting noise of the pyroelectric detector is therefore amplifier noise.

The structure of a typical pyroelectric detector is shown in figure 30. A thin film of mylar whose upper surface is metallized, is

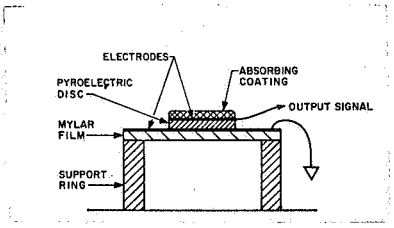

Figure 30 Construction of a pyroelectric detector

stretched over a support ring. A thin disc of the pyroelectric material, with gold electrodes evaporated onto both surfaces, is attached to the mylar film with conducting cement. The upper surface of the disc is blackened. The signal is taken off the upper electrode while the lower one in contact with the metallized mylar is grounded.

Although no information on spatial sensitivity could be obtained from the manufacturer, it seems that it will depend mainly on the uniformity on black coating. Therefore very uniform responsivity should be obtainable provided the crystal itself is uniform. So far pyroelectric detectors have been manufactured in sizes of $(0.1 \times 0.1)\,cm^2$ but reference 17 says that sizes of $(1 \times 1)\,cm^2$ are

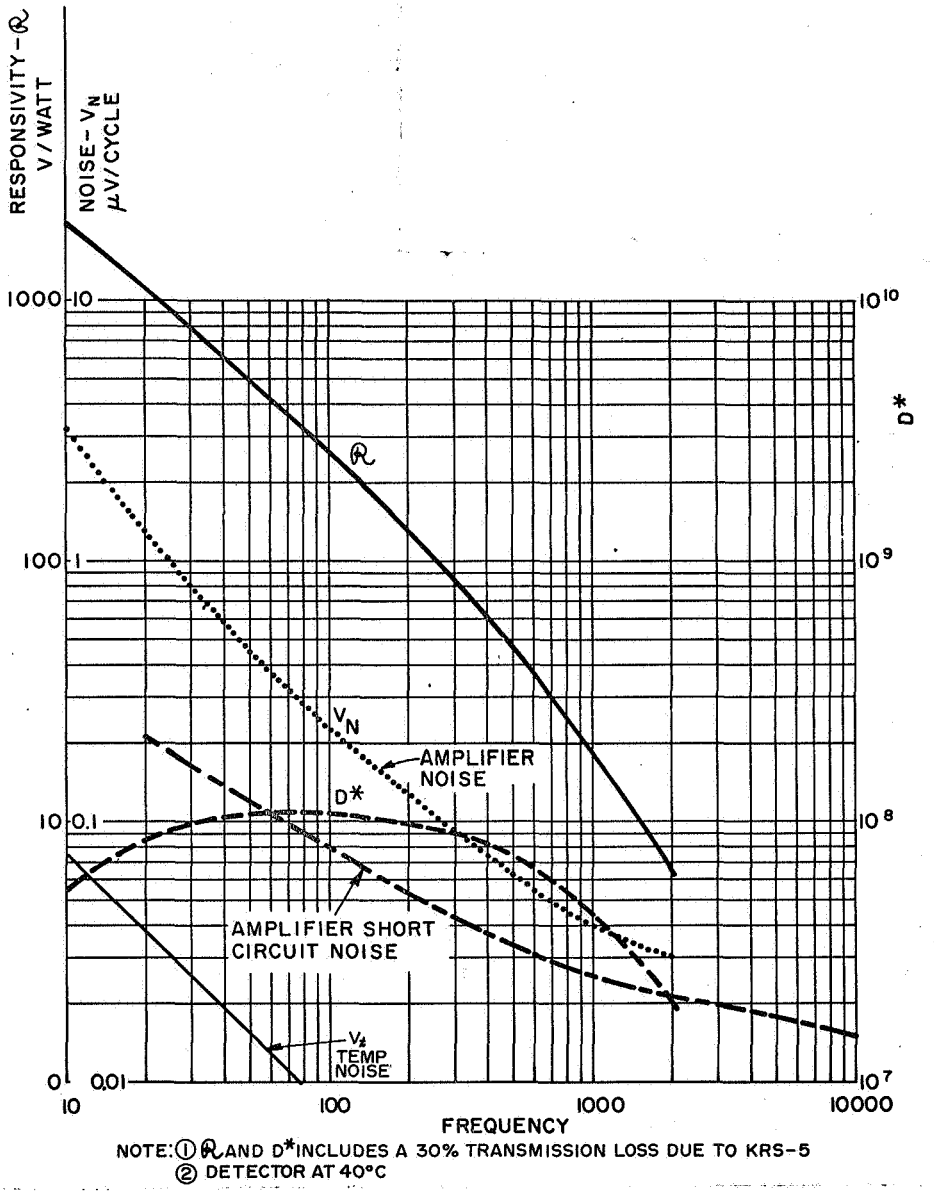

Fig. 31. Responsivity, detectivity and noise vs. frequency for TGS pyroelectric detector.

possible. Dunn Associates has recently received a quotation on a pyroelectric detector with a sensitive area of (1.2 x 1.2)cm^2.

Characteristics of a typical (0.1 x 0.1)cm^2 triglycine sulfate pyroelectric detector are shown in figure 31. It gives a plot of the responsivity, noise and D* as functions of modulation frequencies. The short circuit noise of the amplifier is also shown and we can see that at about 1000 cps this noise becomes predominant and D* falls rapidly thereafter. The specific detectivity (D*) is 10^8 up to 200 cps. This includes a 30% transmission loss for the KRS-5 window employed.

Those detectors described above, at least to our knowledge, show the best qualities of all commercially available ambient temperature detectors* which can be used with the Fourier spectrometer-EMR system. After discussing the cooled detectors we will choose the best suitable ambient temperature detector and investigate its expected performance in the system.

3.3.2 Cooled Detectors

As was the case for the section about ambient temperature detectors, this section is not intended to give a complete survey of all cooled detectors. We will only list detectors which will at least span the wavelength range of one of the interferometers. If there are more than one detector covering the same wavelength range, we will pick the one which seems better suited for our purpose.

Before we discuss specific detectors it seems necessary to make some general remarks. By cooling a detector the internal detector noise becomes very small up to a point where the noise, caused by random fluctuations in background photons striking the detector,

---

*The large area bolometer described in reference 19 which would have many desirable qualities has been excluded because it is not commercially available.

becomes dominant. This photon noise is proportional to the square-root of the incident photon rate. Since the incident photon rate is proportional to effective weighted solid angle ($\bar{\Omega} = \pi \sin^2 \theta_2$ for diffusely viewing detectors; see page 38), the photon noise is proportional to the sine of half angle of the cone. This is expressed in the relationship

$$D^*(\theta) = \frac{D^*(\pi)}{\sin(\theta/2)}$$

where $D^*(\theta)$ is the value of D^* at angle θ, $D^*(\pi)$ is the value of D^* when $\theta = \pi$, and θ is the total cone angle of the incident radiation. Figure 32 shows a plot of that function.

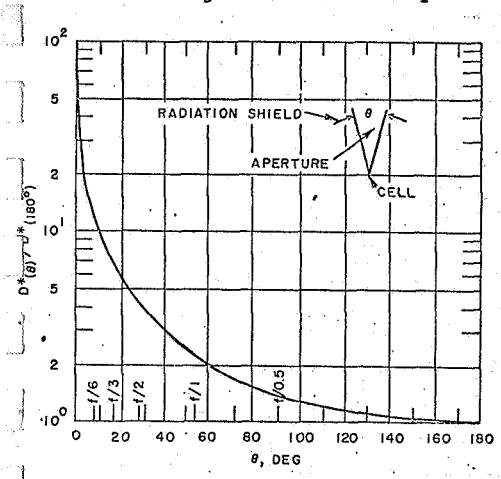

Figure 32. Relative theoretical change in D* by using a cooled aperture in front of the detector.

From figure 32 we see that we could expect an increase in D* by a factor of 2 by using a cooled aperture limiting the field of view to 60°. Actual measurements of D* and D** show that above theoretical relationship holds down to total cone angles of about 30°, where internal noise becomes dominant again. D** is defined as

$$D^{**} = D^*(\theta)\left(\frac{\bar{\Omega}}{\pi}\right)^{\frac{1}{2}}$$

which for a diffuse viewing detector becomes identical to the previous equation. D** can be interpreted as a view field independent detectivity. Figure 33, taken from reference 20, shows the results of measurements of D* and D** as a function of the total cone angle.

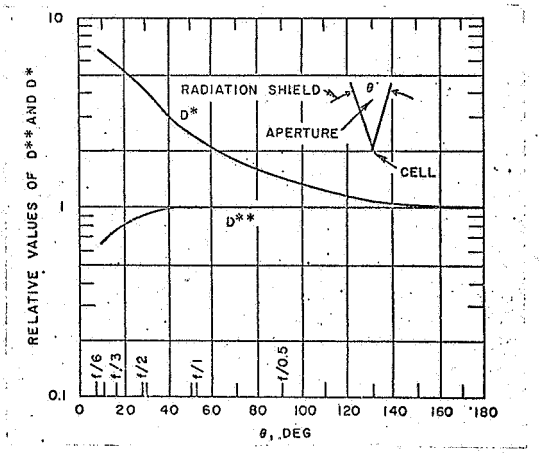

Fig. 33. Relative change in D** achieved by using a cooled aperture in front of a detector.

Reference 20 contains a very informative plot of the maximum D* obtainable at any wavelength with an average detector regardless of its operating temperature. This plot is shown as Figure 34.

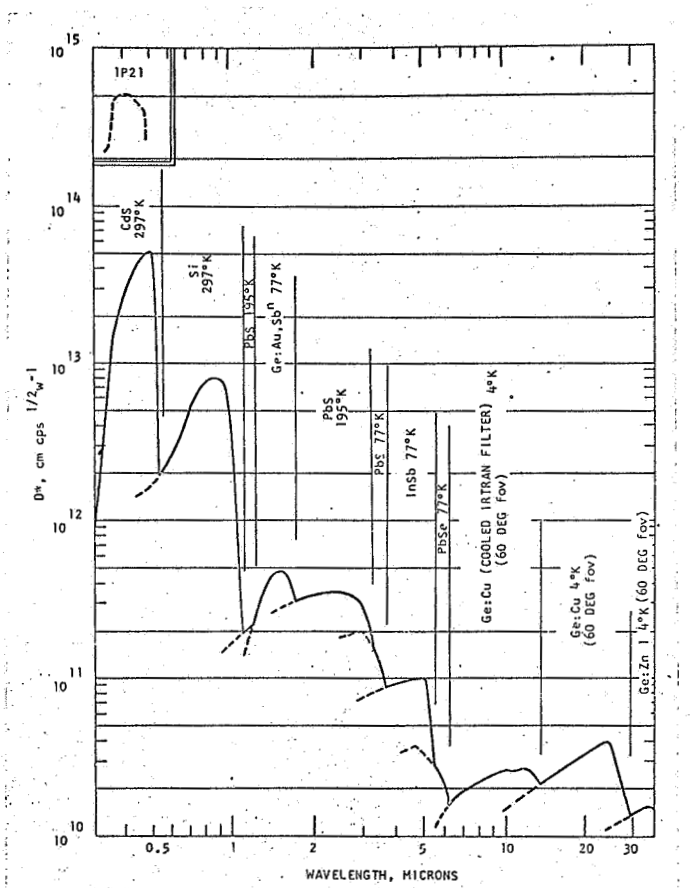

Fig. 34. Maximum D* obtainable with average detectors regardless of operating temperature.

Figure 34 also shows that detectors available for the IR have a much lower D* than those for the visible region of the spectrum.

3.3.2.1 The Mercury Cadmium Telluride Detector

Most of the information about this detector has been or still is classified. Recently, however, an article* appeared which shows some parameters of this detector.

The HgCdTe sensor is operated at liquid nitrogen (77°K) temperature. It covers the wavelength range from 2 to 14μm with a peak specific detectivity (D*) between 10^9 and 10^{10} cm $(cps)^{\frac{1}{2}}$/Watt. It is a very fast detector with a time constant around 10 nanoseconds. The sensitive area ranges from 0.003 to $1mm^2$. Table 4, taken from the article mentioned above, shows some parameters of HgCdTe detectors produced by different manufacturers.

Table 4

HgCdTe DETECTOR CHARACTERISTICS

MANUFACTURER	Société Anonyme de Télécommunications (SAT) Paris, France U.S. Mfg. Rep: Eltek Corp. Larchmont, N.Y.	Honeywell Inc. Research Center Boston, Mass.	Santa Barbara Research Center Goleta, Calif.
PART NUMBER	4 541 015 (in glass dewar) 4 541 016 (in metal dewar)	IR603	Experimental
DETECTOR TYPE	Photovoltaic	Photoconductive	Photoconductive
PEAK SPECTRAL DETECTIVITY (D*)	$10^9 - 10^{10}$ cm(Hz)½/W	>4 x 10^9 cm(Hz)½/W	10^9 cm(Hz)½/W
RESPONSE TIME	<10 nanosec. (running as low as 3 nanosec.)	10 nanosec. Strong Targets; 500 nanosec. Weak Targets	5–150 nanosec.
CELL AREA	0.5–1 mm²	.25 mm²	.003–.25 mm²
SPECTRAL RESPONSES AVAILABLE	2–14 μ	10–11 μ	9–11 μ
OPERATING TEMP.	Liquid N₂ (77°K)	Liquid N₂ (77°K)	Liquid N₂ (77°K)
IMPEDANCE	5–50 Ω	20–300 Ω	30–300 Ω
WINDOW	Irtran II or anti-reflection coated germanium	Irtran II	Irtran II
FIELD OF VIEW	30°	60°	Built to customer requirements

*Joel A. Strasser, NASA Receives French IR Detector, Aerospace Technology, Feb. 12, 1968.

This detector would cover the wavelength range of model 196-T interferometer. Its main disadvantages are the small sensitive area and the narrow field of view.

3.3.2.2 The Mercury doped Germanium detector (Ge:Hg)

The mercury doped germanium detector is a single crystal photoconductive detector for the 2 - 14μm region. It is 300°K background limited when operated below 40°K. Figure 35, taken from reference 20, gives D^*_λ of Ge:Hg detectors at 4°K. Also shown as comparison is the D* of copper doped germanium detectors. It should be noted that the D* of Ge:Hg varies with area, small area detectors having higher values. Table 5, taken from reference 21, shows this quite clearly.

Table 5

D* of Ge:Hg for Several Fields of View

Field of View	D*(500,1000,1)	
	$A < 2 \times W^{-3}cm^2$	$A > 2 \times 10^{-3}cm^2$
120°	7×10^9	4×10^9
80°	9.5×10^9	5.5×10^9
40°	1.8×10^{10}	1×10^{10}
20°	3.5×10^{10}	2×10^{10}

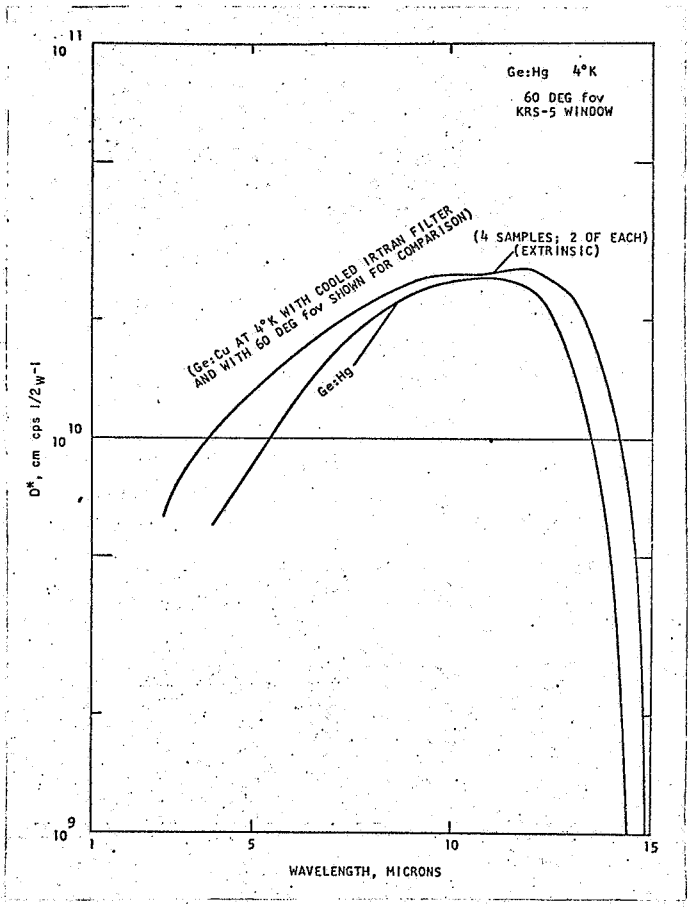

Fig. 35. D^*_λ for mercury doped germanium detector

Ge:Hg detectors are manufactured in sizes up to (0.5 x 0.5)cm^2. The time constant is 0.5μ sec for temperatures 20°K. The responsivity depends on the field of view as well as on the sensitive area of the detector. Figure 36, taken from reference 21, shows this dependency.

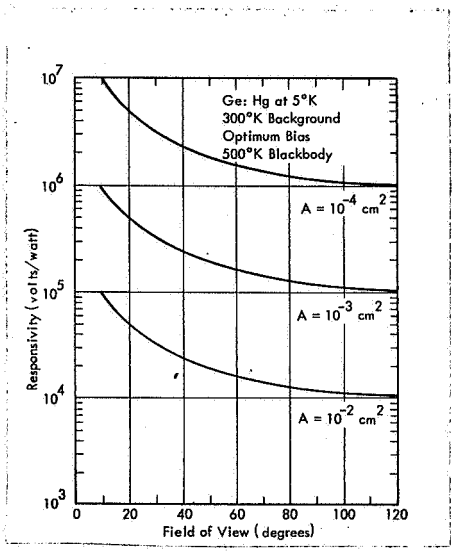

Figure 36. Open circuit 500°K blackbody responsivity versus field-of-view at 5°K for several detector areas.

3.3.2.3 The Zinc doped germanium detector.

This detector, also known as the ZIP detector (zinc impurity p-type), has the widest wavelength range of all doped germanium detectors. It has a D* of about 1 x 10^9 at 2μm and reaches 2 x 10^{10} at about 37μm. Its cutoff wavelength is between 38 and 40μm. Figure 37, taken from reference 20, gives D^*_λ for an average Ge:Zn detector.

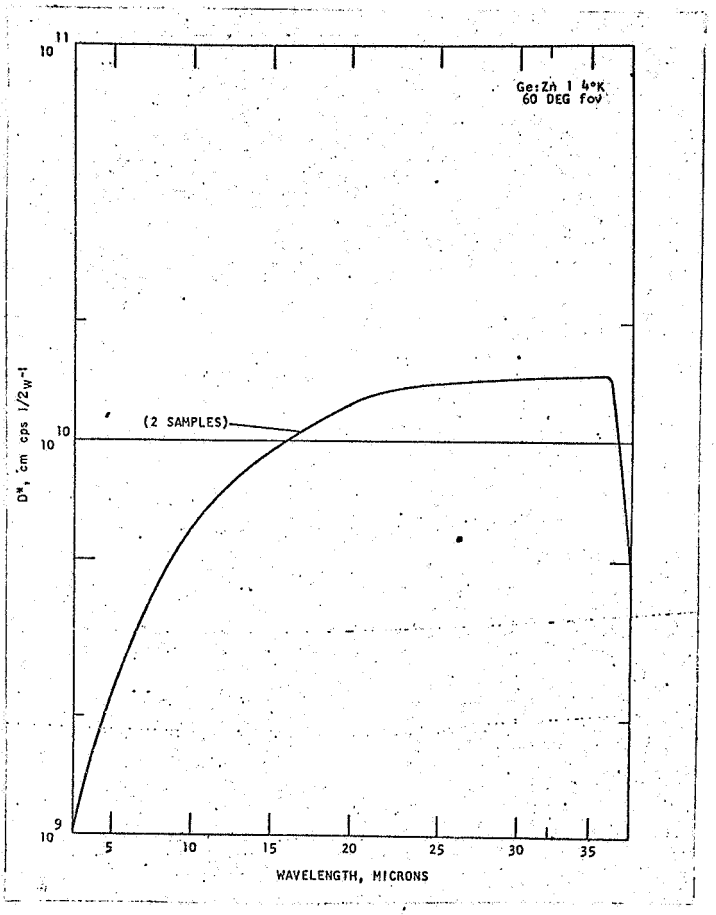

Figure 37. D^*_λ for an average Ge:Zn detector.

The Ge:Zn detector has to be operated at liquid helium temperature (4.2°K). It has a time constant of less than 1μ sec. It is commercially available in sizes up to (0.5 x 0.5)cm^2. Dunn Associates has received a quotation from Texas Instruments at Dallas, Texas, on a Ge:Zn detector with a sensitive area of (1.2 x 1.2)cm^2. However, Texas Instruments was not willing to guarantee the requested specifications "due to the large size of the element and prototype nature of the device."

3.3.2.4 The Gallium doped Germanium Bolometer

This cryogenic bolometer, developed at Texas Instruments, Incorporated, has been described in several papers.[22,23,24] Being a thermal detector the time response can be varied by changing the dimensions and construction of the detector. An increase in time constant means also an increase in responsivity. Low[22] reports that the time constant of the bolometer at 2°K is variable from less than 10^{-5} sec to many seconds, and that the responsivity can exceed 10^5 Volts/Watt. At 4.2°K, a field of view of 180°, and a background temperature of 300°K the detector is background limited. At small apertures this condition can only be achieved by cooling the sensitive element below 4.2°K. Figure 38, taken from reference 22, shows values of calculated noise equivalent power together with

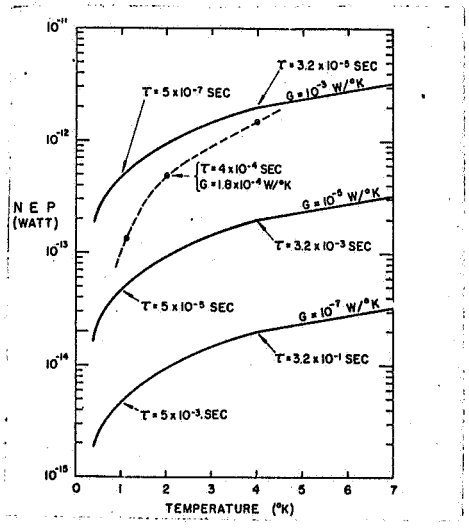

Fig. 38. Calculated temperature variations of NEP and measured values for a typical bolometer. (thickness t=10μ, sensitive area a=0.1cm^2.)

experimental results. G is the thermal conductance between bolometer element and bath.

Germanium bolometers have been built in sizes from (0.06 x 0.025)cm^2 to (0.5 x 0.5)cm^2. Texas Instruments, Inc.* was willing to make a bolometer to our specifications on a trial basis. The expected NEP at a modulation frequency of 25 cps (corresponding to a wavelength of 40μm) was 1 x 10^{-9} Watts. A sensitive area of (0.5 x 0.5)cm^2 would have been used with a cooled image reducing light cone in front of the element. Table 6, taken from a sales brochure of TI, shows the specifications of typcial germanium bolometer systems.

Table 6

Specification for typical germanium bolometers

SPECIFICATIONS	1	2	3	4	5	6	7	8	9	10	11	12	13	14	15
Spectral Region (microns)	8–14	1–20	100–1500	50–	50–	8–14	2–12	2.4 mm	8–14	50–	20–55	45–200	40–250	50–500	12–100
Chopping Speed (Hz)	35	20	10	11	13	10	20	30	35	13	13	13	13	16	13
Operating Temp. (° Kelvin)	2.0°	2°	2°	4.2°	4.2°	4.2°	4.2°	4.2°	2°	4.2°	4.2°	4.2°	4.2°	1.5°	4.2°
Detector Area (mm x mm)	1x.6	1x5	5x5	2x2	5x2	2x2	5x5	5x5	.6x.25	2x2	2x2	4x4	2x2	5x5	1x1
Cone Angle	15°	53°	15°	15°	23°	4°	90°	wave guide	15°	light pipe 10°	light pipe 13°	light pipe 4.0°	60°	15°	10°
N E P (watts x 10^{-13})	5	30	30	10	30	10	500	5000	5	30	200	30	100	8	10

*Private communication with Mr. J.B. Damrel, Jr. of Texas Instruments, Inc. at Houston, Texas.

3.3.3 Conclusions

Of all ambient temperature detectors investigated, the pyroelectric detector from Barnes Engineering seems to offer the greatest advantages for the use with the ellipsoidal mirror reflectometer. It can be manufactured in sizes large enough to receive the complete image at the second focal point and, although not proven experimentally, should be spatially insensitive enough to eliminate the need for an averaging device. For these reasons it would be highly desirable to experimentally investigate the performance of a large area pyroelectric detector with a Fourier spectrometer-EMR system. Dunn Associates has received a quotation from the Barnes Engineering Company on such a detector, with a sensitive area of $(1.2 \times 1.2)cm^2$. The noise equivalent power at 25 cps was expected to be less than or equal to 1×10^{-8} Watts. Unfortunately the purchase price of $6,758., which would include the development cost for the large area element, is well beyond the funds available for this study program. For this reason, as well as the long delivery time involved, Dunn Associates is unable to make an experimental evaluation.

Assuming that the pyroelectric detector would meet the specification, we can calculate the measurement time necessary to obtain a given signal to noise ratio. From figures 20 and 21 we find that the lowest flux level occurs at 40μm. The flux level at 40μm was calculated as 1×10^{-7} Watts using a sample reflectance of 10%. To obtain an accuracy of 1% full scale we should have a signal to noise ratio of 500. The signal to noise ratio is given by

$$\left(\frac{S}{N}\right)_\lambda = \frac{\Phi_\lambda}{NEP}.$$

Φ_λ at 40μm and for a 100% reflectance is 1×10^{-6} Watts

NEP is 1×10^{-8} Watts.

With this $\left(\frac{S}{N}\right)_{40} = \frac{1 \times 10^{-6}}{1 \times 10^{-8}} = 100$. This represents the signal to noise ratio for a measurement time of 1 second. Since S/N is proportional to the square root of the measurement time τ, the time to achieve a S/N of 500 is given by $\tau = (500/100)^2 = 25$. In other words, we can achieve a S/N of 500 by coherently adding 25 interferograms. If detector scanning should become necessary S/N would drop by a factor of 0.25 or S/N = 125. To bring it back up to a level of 500 we would have to increase the measurement time by another factor of 16. The total measurement time would then become (25)(16) = 400 sec. This is still reasonable. So, we can say that the measurement looks indeed feasible if the pyroelectric detector meets its specifications.

The most attractive detector of the cooled detectors seems to be the Ge:Zn detector. It could be used over the entire wavelength region of the two interferometers, or at least out to 38μm. Providing that the large area of 1.44 cm^2 Ge:Zn detector would meet the specifications the S/N would be improved by almost two orders of magnitude over the pyroelectric detector. On the other hand it would impose the inconvenience of liquid helium cooling with the requirement of installing a fairly bulky (16 cm diam; 39 cm high) cryogenic dewar.

3.4 Correction for systematic errors.

A very detailed analysis of systematic as well as random errors connected with reflectance measurements by an ellipsoidal mirror reflectometer has been performed by Dunn[25] and will not be repeated here. The basic idea was to make very accurate corrections on large errors, such as the entrance hole loss, and to make a rough estimate on small errors, since a large error in a small correction causes only a small error in the end result. We will give an alternate and more accurate approach to correct for the entrance hole loss. Dunn had to

assume that the flux density at any point within the entrance hole was the same as on the ellipsoidal mirror next to the entrance hole. This assumption is probably good enough if the entrance hole is small. It becomes certainly questionable in our case because we decided to allow a 3% entrance hole loss (based on a perfectly diffuse reflector) in order to take at least some advantage of the large throughput of the interferometer.

The error caused by that portion of the reflected flux which escapes through the entrance port will be essentially zero for the specular reflectance standard and will become a maximum for materials which backscatter into the direction of incidence. The flux leaving the ellipsoidal mirror through the entrance hole could be measured by means of a beamsplitter as indicated in figure 38.

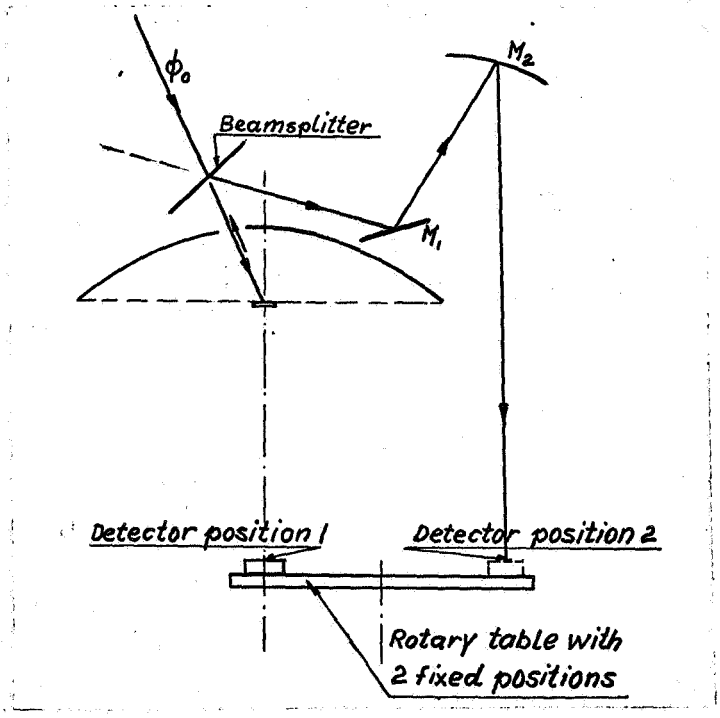

Fig. 38 Measurement of the flux lost through the entrance hole.

The beamsplitter is placed in front of the entrance hole. Of the monochromatic flux ϕ_0, which is incident on the beamsplitter, the fraction τ_B is transmitted down to the sample. The flux reflected by the sample is then $\tau_B \rho_S \phi_0$. A fraction, f_H, of the reflected flux escapes through the entrance hole, is partially reflected by the beamsplitter and reaches the detector in position 2 via a flat and a spherical mirror. The signal, S_3, obtained from the detector would be

$$S_3 = C \tau_B \rho_S f_H \rho_B \rho_1 \rho_2 \phi_0 \ ,$$

where C is a proportionality constant

τ_B is the transmittance of the beamsplitter

ρ_S is the reflectance of the sample

f_H is the fraction of the reflected flux lost through the entrance hole

ρ_B is the reflectance of the beamsplitter

ρ_1, ρ_2 are the reflectances of M_1 and M_2 respectively

(Note: all properties are monochromatic properties.)

The signal S_2, obtained with the beamsplitter removed, the sample replaced by a specular reflectance standard and the detector in position 1 is

$$S_2 = C \rho_{ST} \rho_E \phi_0 \quad \text{or} \quad \phi_0 = \frac{S_2}{C \rho_{ST} \rho_E} \ ,$$

where ρ_{ST} is the reflectance of the specular standard

ρ_E is the reflectance of the ellipsoidal mirror.

Substituting the expression for ϕ_0 into the equation for S_3 we obtain f_H as

$$f_H = \frac{S_3}{S_2} \frac{\rho_{ST} \rho_E}{\tau_B \rho_S \rho_B \rho_1 \rho_2} \ .$$

This means that we need to know the transmittance and reflectance of the beamsplitter as well as the reflectances of the mirrors involved to obtain f_H .

We should be aware that the signal to noise ratio in S_3 will be drastically lower than in our previous calculations. Assuming an ideal beamsplitter and a diffuse reflector with a reflectance of 1 the flux level on the detector would be $0.25(0.03)\,\phi_\lambda = 0.0075\,\phi_\lambda$. Or the signal to noise ratio is more than two orders of magnitude lower than in our previous calculations. However, the hole loss is only a function of the directional distribution of the reflected flux, which changes very slowly with wavelength. Therefore one could use the data obtained at wavelengths, where sufficient energy is available and use those to correct the data at other wavelengths.

4.0 Summary

In this report we have studied the problems associated with a Fourier Spectrometer-Ellipsoidal Mirror Reflectometer system. One of the most important problems was to find a suitable averaging technique which could be used efficiently at long wavelengths. The result was that at long wavelengths, where the system becomes energy limited, detector scanning is the clear choice because of its superior efficiency.

Another problem studied was the compromise between using the large throughput of the interferometer and the error caused by the large entrance hole in the ellipsoidal mirror. The conclusion was that one will have to accept a fairly large error in the basic measurement to allow sufficient energy to enter the system. Additional measurements will, however, be required to make corrections for the errors to ensure that the error in the final result will be less than 0.01. Flux levels were calculated using parameters of model 196T and 196TC Block interferometers. As could be expected, the crucial region was the long wavelength region, where the radiant power, based on certain assumptions, fell to 1×10^{-7} Watts.

Keeping this in mind, we took a look at all available detectors which showed at least some promise of success. Detectors used at ambient temperature as well as cooled detectors were investigated. The most interesting ambient temperature detector turned out to be a recently developed pyroelectric detector. A quotation for such a detector with a sensitive area of $(1.2 \times 1.2)\text{cm}^2$ was obtained from Barnes Engineering. This detector has a NEP of 1×10^{-8} Watts at 25 cps (corresponding to 40μm). The most attractive feature of this detector is that it could, at least theoretically, be used without an averaging device. This would have to be established experimentally. Of the cooled detectors, a liquid Helium cooled zinc doped germanium detector would be the choice for our system. It can essentially

cover the entire wavelength range of the two interferometers and its D* peaks at about 37μm where the detectable radiant power has almost reached its lowest level.

Because of the limited funds available for this study program, and also because of time limitations, the two detectors mentioned above could not be evaluated experimentally. At this time we would, however, like to mention that Dunn Associates has started to build a prototype of a system, which, except for accuracy specification, will be exactly the system discussed in this report. During this development program, which is planned to last six months, Dunn Associates will buy one or possibly even both detectors discussed above and will test them thoroughly. At the end of that experimental program Dunn Associates will supply NASA with the results of the detector evaluation. Since the development program has the funds and also the time necessary to procure and test the detectors in an actual reflectometer system, it is our opinion that the results will be of much greater value than those which could have been obtained within the limitation of this study contract.

A final word about the meaning of 0.01 accuracy of reflectance measurements. Sometimes the reflectance measurements are used to obtain the emittance of materials by using the equation $\varepsilon(\theta) = 1 - \rho(\theta; 2\pi)$, where $\varepsilon(\theta)$ is the directional emittance and $\rho(\theta; 2\pi)$ is the directional, hemispherical reflectance as measured by the ellipsoidal mirror reflectometer. The first problem we face is that for highly reflective materials an error of 0.01 in reflectance translates into a very large error in emittance. For example, if we have $\rho = 0.98 \pm 0.01$ the emittance will be between 0.03 and 0.01. This means that for low emitters the emittance obtained from reflectance measurements will be very inaccurate. A direct measurement of emittance might therefore be a more useful approach.

A second problem is that for heat transfer analysis the quantity

really needed is the hemispherical emittance whereas the quantity obtained from the measurement of directional, hemispherical reflectance is the directional (mostly near normal) emittance. One would have to measure the reflectance at all angles of incidence and integrate them to obtain bihemispherical reflectance which corresponds to hemispherical reflectance. This can be done up to polar angles of 50° or more, but at very large polar angles it becomes increasingly difficult or impossible to take reflectance measurements. Therefore one has to make a guess at the reflectance at large polar angles, which, as pointed out by Millard,[26] can lead to great errors.

As a result of this short discussion, an accuracy of 0.01 in directional, hemispherical reflectance is not sufficient if the desired quantity is the hemispherical emittance, and this is especially true if highly reflective surfaces are concerned.

REFERENCES

1. Connes, J., Rev. Optique, 1961, pp. 40,45,116,171,231. An English translation is available from the Defense Documentation Center, AD 490 869.

2. Mertz, L., Transformation in Optics, John Wiley & Sons, New York, 1965.

3. Chaney, L.W., "Fundamentals of Fourier Transform Spectroscopy," Technical Report of the University of Michigan, 1967. NASA Report No. CR 84119.

4. Dunn, S.T., Richmond, J.C., and Wiebelt, J.A., "Ellipsoidal Mirror Reflectometer," J. Res. Natl. Bur. Std., Vol. 70C, No. 2, pp. 75-88, 1966.

5. Dunn, S.T., "Flux Averaging Devices for the Infrared," NBS Technical Note No. 279, 1965.

6. Finkel, Mitchell W., "Uniform Local Responsivity of Detectors by Scanning," Report of the Goddard Space Flight Center, Greenbelt, Md., No. X-713-67-537, Nov. 1967.

7. Dunn, S.T., "Interferometer Spectrometer Used as an Optical Chopper," Applied Optics, Vol. 6, p. 1780, Oct. 1967.

8. Geist, Jon and Kneissl, G., "Detector Scanner for Accurate Radiometric Measurements," Paper at the Fall, 1967 Meeting of the Optical Society of America.

9. Ferriso, Carmine C., "Blackbody Radiation Tables," AD 291 200, September 1962.

10. Jamieson, John A. et al., Infrared Physics and Engineering, McGraw-Hill Book Co., Inc., 1963.

11. Wolfe, William L., Editor, Handbook of Infrared Technology, Office of Naval Research, Department of the Navy, Wash., D.C.

12. Infrared Components, Santa Barbara Research Center Brochure No. 676M, Santa Barbara Research Center, Goleta, California.

13. Stair, Ralph, Schneider, William E., Waters, William R., and Jackson, John K., "Some Factors Affecting the Sensitivity and Spectral Response of Thermoelectric (Radiometric) Detectors," Applied Optics, vol. 4, page 703, June, 1965.

14. Holter, Marvin R. et al., Fundamentals of Infrared Technology, The MacMillan Company, New York, 1963.

15. Astheimer, Robert W. and Weiner, Seymour, "Solid-Backed Evaporated Thermopile Radiation Detectors," Applied Optics, vol. 3, No. 4, April, 1964.

16. Barnes Engineering Company, Bulletin 2-212, "Thermopile Radiation Detectors," Stamford, Connecticut, May 9, 1966.

17. Astheimer, Robert W. and Beerman, Henry P., "The Pyroelectric Detector," internal publication of the Barnes Engineering Co., Stamford, Connecticut.

18. Beerman, Henry P., "Pyroelectric Infrared Radiation Detector," The American Ceramic Society Bulletin, Vol. 46, No. 8, Aug. 1967.

19. Blevin, W.R. and Brown, W.J., "Large-area Bolometers of Evaporated Gold," J. Sci. Instrum., vol. 42, pages 19-23, 1965.

20. Gorrono, Bruno G., "A Compilation of Photodetectivity Parameters," Report of the U.S. Naval Ordnance Test Station, China Lake, California, AD 477387, Feb. 1966.

21. Infrared Devices, Texas Instruments Incorporated, Dallas, Texas.

22. Low, Frank J., "Low-Temperature Germanium Bolometer," JOSA, vol. 51, No. 11, November 1961.

23. Low, F.J. and Hoffmann, A.R., "The Detectivity of Cryogenic Bolometers," Applied Optics, vol. 2, June 1963.

24. Jones, Charlie E. Jr., Hilton, A.R., Damrel, J.B. Jr., and Helms, C.C., "The Cooled Germanium Bolometer as a Far Infrared Detector," internal publication of Texas Instruments, Inc., Dallas, Texas.

25. Dunn, S. Thomas, "Design and Analysis of An Ellipsoidal Mirror Reflectometer," Ph.D. Thesis, Oklahoma State University, May, 1965.

26. Millard, John and Streed, Elmer, "A Comparison of Infrared Emittance Measurements and Techniques," presented at the 1968 Spring Meeting of the OSA, Washington, D.C., March, 1968.